A domain decomposition approach for the simulation of fracture phenomena in polycrystalline microsystems

Federica Confalonieri, Aldo Ghisi, Giuseppe Cocchetti, Alberto Corigliano*

Dipartimento di Ingegneria Civile e Ambientale, Politecnico di Milano, Piazza Leonardo da Vinci 32, 20133 Milano, Italy

Received 28 December 2013; received in revised form 4 April 2014; accepted 15 April 2014
Available online 30 April 2014

1. Introduction

This work focuses on a domain decomposition approach to the 3D finite element simulation of crack initiation and propagation in polycrystalline materials via a cohesive methodology. The main application is the numerical modelling

* Corresponding author. Tel.: +39 0223994244; fax: +39 0223994300.
E-mail address: alberto.corigliano@polimi.it (A. Corigliano).

of the mechanical behaviour of polycrystalline silicon in microsystems. Polysilicon displays indeed a quasi-brittle behaviour at room temperature: consequently, as underlined in [1] and [2], the reliability of microsystems is often affected by rupture phenomena, due for instance to impacts or accidental shocks. In particular, the analysis refers to the microscale level, i.e. to the microstructural parts composing the MEMS device, which may be subjected to local failure phenomena.

Polysilicon is an aggregate of mono-crystalline silicon grains, whose overall behaviour is sensibly influenced by the mechanical properties of the grains and of the grain boundaries, by their shape and orientation. At this scale, the overall behaviour is strongly influenced by the material microstructure and the models have to take into account the presence of heterogeneity, interfaces between grains and micro-cracks. Consequently, any computational model for the prediction of its microscale behaviour must properly reproduce the grain morphology and the grain boundaries, which strongly influence the resulting mechanical response. As a result, a very refined discretization is required to reproduce the grain geometry. The computational burden of a traditional finite element simulation of the mechanical response of polycrystalline solids, under impact dynamics and in the presence of crack-propagation, is indeed very high, especially in the three dimensional case: the explicit time step is ruled by the Courant–Friedrichs–Lewy (CFL) condition and it could be very small, since a very refined spatial discretization is often required to properly mesh the grain boundaries and to solve the cohesive process zone.

A domain decomposition technique, described in the following section, is proposed in this work to overcome this limitation. The basic idea of domain decomposition techniques, as suggested by the name itself, lies in the subdivision of the global domain into subdomains to be solved separately and then reconnected by interface conditions. These approaches naturally apply to the solution of problems of great size; their goal is indeed to significantly increase the computational efficiency of the numerical simulations. The algorithm here described starts from the dual Schur's domain decomposition method for the solution of the dynamic problem, developed by Gravouil and Combescure [3] and Mahjoubi et al. [4], as an extension of the Finite Element Tearing and Interconnecting Method (FETI), originally proposed by Farhat and Roux [5] for the multi-domain and parallel solution of the elastostatic problem. In the literature, domain decomposition techniques have been recently applied e.g. by Lloberas-Valls et al. [6] and by Pebrel et al. [7] to the study of localized damage phenomena under static loading conditions and by Kerfriden et al. [8] to the analysis of delamination in composite materials. A survey of the state of the art on domain decomposition methods can be found in [9] and in [10]. The introduction of a domain decomposition approach allows for a sensible reduction of the number of degrees of freedom for each subdomain with respect to those of the whole domain and for a more efficient handling of the time integration, thus reducing the computational burden. The aims are to exploit smaller sub-problems and to overcome the time-step limits encountered with the standard description in an explicit dynamic scheme (i.e. the CFL condition).

The present paper contains a comprehensive description of the domain decomposition approach for fracture propagation in polycrystalline solids that has already been partially described in [11] with specific reference to microsystems applications. The proposed approach includes: the use of a Voronoi tessellation algorithm for the reproduction of the polycrystalline micro-structure; interface, cohesive laws for the description of fracture processes; dynamic insertion of interface Finite Element (FE) and relevant topology modification of the FE mesh; a new domain decomposition multi-time step strategy that allows for fracture propagation inside, at the boundary at across sub-domains; various strategies for domain partition. In the literature, cohesive models were extensively used for the numerical simulation of the mechanical fracture properties of microstructured materials with different numerical techniques [12–18].

The paper is organized as follows. In Section 2 the reference problem is introduced; Section 3 is devoted to the description of the proposed algorithm. Various partition techniques are discussed in Section 4. Section 5 contains a collection of numerical examples; closing remarks are proposed in Section 6.

2. Reference problem

The reference problem, shown in Fig. 1, can be formulated considering a continuum three-dimensional body Ω crossed by a propagating discontinuity surface Γ_c and subjected to dynamic loading conditions. The outer boundary of the body is partitioned into two portions $\partial\Omega_f$ and $\partial\Omega_d$, such that $\partial\Omega_d \cap \partial\Omega_f = \varnothing$ and $\partial\Omega_d \cup \partial\Omega_f = \partial\Omega$: surface forces $\mathbf{f}$ and displacements $\bar{\mathbf{u}}$ are assigned respectively on $\partial\Omega_d$ and $\partial\Omega_f$. Body forces, collected in the vector $\mathbf{b}$, are assigned in $\Omega\backslash\Gamma_c$. The two flanks of the crack are referred to as Γ_c^+ and Γ_c^-.

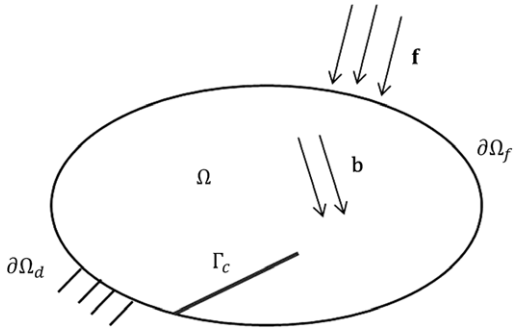

Fig. 1. Elastic continuum subject to fracture.

Let $\mathbf{u}$ and $\ddot{\mathbf{u}}$ be the displacement and the acceleration vector field and σ and ε the stress and strain tensors in $\Omega\backslash\Gamma_c$.

A linearized kinematics is assumed. The bulk body material is assumed to obey a linear elastic constitutive law, while a cohesive law is introduced at the interface Γ_c to model the decohesion between the two sides of the crack. The mechanical behaviour of the body in the time range $[t_0, t_f]$ is governed by the following set of equations:

$$\mathbf{div}(\sigma) + \mathbf{b} = \rho\ddot{\mathbf{u}} \quad \text{in } \Omega\backslash\Gamma_c,\ t \in [t_0, t_f] \tag{1a}$$

$$\sigma = \mathbb{C} : \varepsilon\,(\mathbf{u}) \quad \text{in } \Omega\backslash\Gamma_c,\ t \in [t_0, t_f] \tag{1b}$$

$$\varepsilon = \frac{1}{2}(\nabla\mathbf{u} + \nabla\mathbf{u}^T) \quad \text{in } \Omega\backslash\Gamma_c,\ t \in [t_0, t_f] \tag{1c}$$

$$\sigma \cdot \mathbf{n} = \mathbf{f} \quad \text{on } \partial\Omega_f,\ t \in [t_0, t_f] \tag{1d}$$

$$\mathbf{u} = \bar{\mathbf{u}} \quad \text{on } \partial\Omega_d,\ t \in [t_0, t_f] \tag{1e}$$

$$[\mathbf{u}] = \mathbf{u}|_{\Gamma_c^+} - \mathbf{u}|_{\Gamma_c^-} \quad \text{on } \Gamma_c,\ t \in [t_0, t_f] \tag{1f}$$

$$\sigma^+ \cdot \mathbf{n}^+ = \mathbf{t} \quad \text{on } \Gamma_c^+ \tag{1g}$$

$$\sigma^- \cdot \mathbf{n}^- = -\mathbf{t} \quad \text{on } \Gamma_c^- \tag{1h}$$

$$\mathbf{t} = A\,([\mathbf{u}], \boldsymbol{\theta}) \quad \text{on } \Gamma_c,\ t \in [t_0, t_f] \tag{1i}$$

$$\mathbf{u}(t_0) = \bar{\mathbf{u}}_\mathbf{0} \quad \text{at } t = t_0 \tag{1j}$$

$$\dot{\mathbf{u}}(t_0) = \bar{\dot{\mathbf{u}}}_\mathbf{0} \quad \text{at } t = t_0. \tag{1k}$$

Eq. (1a) expresses the dynamic equilibrium of the body, being ρ the bulk mass density. The linear elastic constitutive law is given in Eq. (1b) for $\Omega\backslash\Gamma_c$. Eq. (1c) represents the linear compatibility between the strain and the displacement field. Static and kinematic boundary conditions are given by Eqs. (1d) and (1e), respectively. Eq. (1i) introduces the interface cohesive law, linking the surface tractions $\mathbf{t}$, acting along Γ_c and defined by Eqs. (1g) and (1h), to the displacement jump, defined by Eq. (1f); A is a generic operator expressing the cohesive tractions as a function of the displacement discontinuity $[\mathbf{u}]$ and of a vector of internal variables $\boldsymbol{\theta}$. Eqs. (1j) and (1k) give the initial conditions for the boundary value problem.

The governing system of relations can be written in weak form through the principle of virtual work. From now on, the stress and the strain field will be expressed in compact Voigt notation, being $\boldsymbol{\sigma}$ and $\boldsymbol{\varepsilon}$ the vectors containing the independent components of the corresponding tensors.

$$\int_\Omega \rho\,\ddot{\mathbf{u}}^T\,\delta\mathbf{u}\,d\Omega + \int_\Omega \boldsymbol{\sigma}^T\,(\boldsymbol{\varepsilon}(\mathbf{u}))\,\delta\boldsymbol{\varepsilon}(\mathbf{u})d\Omega + \int_{\Gamma_c} \mathbf{t}^T\,([\mathbf{u}])\,\delta[\mathbf{u}]\,d\Gamma$$
$$= \int_\Omega \mathbf{b}^T\,\delta\mathbf{u}\,d\Omega + \int_{\partial\Omega_f} \mathbf{f}^T\,\delta\mathbf{u}\,dS \qquad \forall\delta\mathbf{u},\ \delta\mathbf{u} = \mathbf{0} \quad \text{on } \partial\Omega_d. \tag{2}$$

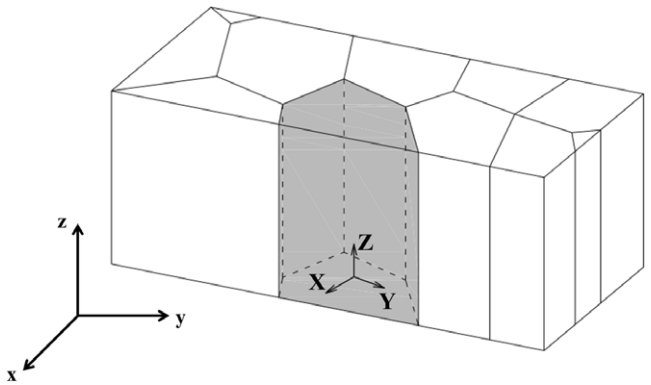

Fig. 2. Global and local reference frames for a polycrystal.

Introducing a displacement-based finite element spatial discretization and considering conforming meshes at the two flanks γ_c^+ and γ_c^- of the crack, the previous equation can be written in semi-discretized form as:

$$\mathbf{M}\ddot{\mathbf{U}}(t) + \mathbf{F}^{\mathbf{int}}(\mathbf{U}(t)) + \mathbf{F}^{\mathbf{cohes}}([\mathbf{U}](t)) = \mathbf{F}^{\mathbf{ext}}(t) \quad t \in [t_0, t_f] \tag{3a}$$

$$\mathbf{U}(t_0) = \bar{\mathbf{U}}_0 \tag{3b}$$

$$\dot{\mathbf{U}}(t_0) = \bar{\dot{\mathbf{U}}}_0 \tag{3c}$$

being $\mathbf{U}$, $\dot{\mathbf{U}}$ and $\ddot{\mathbf{U}}$ the nodal displacement, velocity and acceleration vectors, $[\mathbf{U}]$ the nodal displacement discontinuity vector along Γ_c, $\mathbf{M}$ the mass matrix, $\mathbf{F}^{\mathbf{int}}$ the internal force vector, $\mathbf{F}^{\mathbf{cohes}}$ the vector equivalent to the tractions acting along the interface Γ_c and $\mathbf{F}^{\mathbf{ext}}$ the external force vector. The presence of cohesive elements results indeed in the additional contribution $\mathbf{F}^{\mathbf{cohes}}$ (where the contributions of each cohesive element are assembled) to the internal virtual work term, independent from those deriving from the bulk material.

Finally, after time discretization, at the generic time step $\left[t_n,\ t_{n+1}\right]$, Eq. (3a) can be written as:

$$\mathbf{M}\ddot{\mathbf{U}}_{n+1} + \mathbf{F}^{\mathbf{int}}(\mathbf{U}_{n+1}) + \mathbf{F}^{\mathbf{cohes}}([\mathbf{U}]_{n+1}) = \mathbf{F}^{\mathbf{ext}}_{n+1} \tag{4}$$

where an index $n+1$ stands for a quantity computed at time instant t_{n+1}.

This general formulation can be easily specialized to deal with the case of a polycrystalline material, like polysilicon. Polysilicon can be indeed considered as constituted by an aggregate of monocrystalline grains, displaying a face-centered cubic lattice. The bulk behaviour has been assumed here as linear elastic. This hypothesis is well in agreement with the experimental results showing the absence of any residual deformation and the brittleness of polysilicon at room temperature. As underlined in the introduction, the overall micromechanical response is sensibly affected by the grain morphology. As a consequence, addressing the finite element simulations of polysilicon requires a preliminary step, in which the polycrystalline microstructure is modelled.

The Voronoi tessellation procedure has been extensively used in the literature for the numerical construction of polycrystalline structures; see, for instance, [13,14,19–25].

As in [1,2,14,22–24,26], a virtual polycrystal is here constructed, by means of a numerical tool based on the Voronoi tessellation algorithm. Moreover, the global mechanical response is anisotropic and depends on the constitutive behaviour associated to each grain. It is reasonable to assume that the constitutive law is constant inside each grain, but can vary from grain to grain. If a privileged local reference frame XYZ aligned with the axes of symmetry of the crystal (see Fig. 2), i.e. with axes respectively at [100], [010] and [001] in Miller indexes notation, is considered, only three independent parameters are sufficient to completely characterize the elasticity tensor of each single grain, since it holds that:

$$E_X = E_Y = E_Z \tag{5}$$

$$\nu_{YZ} = \nu_{ZX} = \nu_{XY} \tag{6}$$

$$G_{YZ} = G_{ZX} = G_{XY}. \tag{7}$$

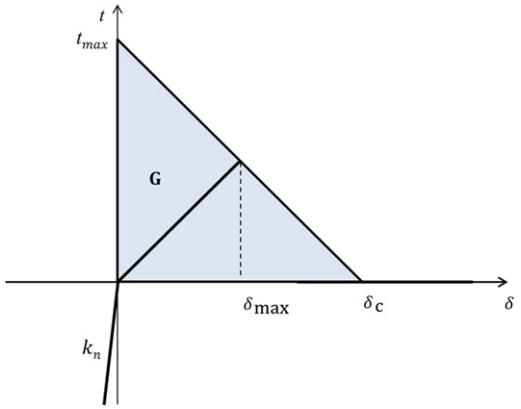

Fig. 3. Effective traction–effective displacement jump interface cohesive law.

The constitutive law in the local reference frame of each single crystal can thus be written as:

$$\boldsymbol{\sigma}^L = \mathbf{S}^L_{grain}\boldsymbol{\varepsilon}^L \tag{8}$$

where $\boldsymbol{\varepsilon}^L$ and $\boldsymbol{\sigma}^L$ are the vectors containing the symmetric components of the stress and the strain tensor in the local reference frame and $\mathbf{S}^L_{grain}$ is the elastic stiffness matrix of the single crystal, that can be written as:

$$\mathbf{S}^L_{grain} = \begin{bmatrix} s_{11} & s_{12} & s_{12} & 0 & 0 & 0 \\ s_{12} & s_{11} & s_{12} & 0 & 0 & 0 \\ s_{12} & s_{12} & s_{11} & 0 & 0 & 0 \\ 0 & 0 & 0 & s_{44} & 0 & 0 \\ 0 & 0 & 0 & 0 & s_{44} & 0 \\ 0 & 0 & 0 & 0 & 0 & s_{44} \end{bmatrix}. \tag{9}$$

In the case of an arbitrary material microstructure, multiple fracture loci can develop and arbitrary crack patterns should be simulated. For this reason, as in [1,2,26], an inter-element formulation is adopted, in which zero-thickness interface elements are inserted between elements' faces, that were perfectly coherent up to the onset of fractures, where an activation criterion is met. Therefore, fracture can develop only along element boundaries. As a result, nucleation, propagation, branching and coalescence of cracks become an outcome of the cohesive approach and do not need to be established a priori. On the other hand, the issue of mesh size dependency is inherited from the inter-element methodology. To avoid mesh dependencies with this standard cohesive approach, it is necessary to control carefully the mesh size along the cohesive crack. In our calculations, the mesh size is calibrated so that at least three integration points are placed along a distance equal to the material characteristic length. The constitutive behaviour of cohesive interface elements is described by a softening law linking the tractions acting at the crack surface to the displacement jump. The linear softening law, developed by Camacho and Ortiz [27] and Ortiz and Pandolfi [28], has been here adopted. This cohesive law, displayed in Fig. 3, is written in terms of the effective scalar variables of displacement jump and traction, respectively defined as:

$$\delta_{eff} = \sqrt{[u]_n^2 + \kappa^2 \left\|[\mathbf{u}]_s\right\|^2} \tag{10}$$

$$t_{eff} = \sqrt{t_n^2 + \frac{1}{\kappa^2}\left\|\mathbf{t_s}\right\|^2} \tag{11}$$

where the subscripts n and s denote the normal and the sliding components of both the opening displacement and the interface traction vectors. The parameter κ acts as a tension–shear coupling factor, weighting the normal and the tangential components. Under monotonic loading condition, the effective cohesive traction is assumed to decrease linearly for increasing displacement jump; it finally reduces to zero when a critical opening displacement δ_c is reached. On the other hand, the model is irreversible: a linear unload to the origin is indeed assumed and the maximum effective displacement jump reached at the integration point $\delta_{\max}$, shown in Fig. 3, acts as a historical variable. The area under

the linear envelope corresponds to the critical fracture energy $G_c = \frac{1}{2} t_{\max} \delta_c$. Two material parameters are sufficient to completely characterize the cohesive law: either the maximum tensile stress $t_{\max}$ and the critical opening displacement δ_c or the maximum tensile stress $t_{\max}$ and the fracture energy G_c.

In the compressive case, i.e. when $[u]_n$ is negative, only the sliding components contribute to the effective opening displacement and a penalty formulation is introduced to handle the contact, modelled as frictionless. A normal interface traction, computed multiplying the normal displacement jump for a conveniently large value of stiffness k_n, is applied to minimize the interpenetration. Crack re-closing brings actually even more complexity to the problem, the approach here followed is only a first approximation.

Since fracture in polycrystalline materials has been shown to occur both inside a grain and at the grain boundary, different values of the maximum tensile stress $t_{\max}$ and of the critical fracture energy G_c are associated to these two cases to distinguish between trans-granular and inter-granular fractures. More refined solutions can be found in the literature. A statistical distribution of grain boundary fracture properties is considered, for instance, in [12,22,29]. In [30–32] the effect of randomly located initial flaws on the overall mechanical behaviour is investigated via a stochastic approach. At the present time, no probabilistic approach has been yet introduced. In the numerical examples here proposed in order to assess the potentiality of the proposed technique, only single realizations of the grain morphology are indeed considered. To obtain more realistic results, probabilistic analyses should be performed, investigating the influence of the stochastic nature of the fracture properties and of the grain morphology, size, and orientation on the mechanical response of the material. Moreover, in the particular case of polysilicon, there are experimental evidences [33] that also the fracture behaviour displays a clear anisotropy inside the grains: the fracture energy depends indeed on the relative orientation between the cohesive zone and the crystal lattice. This aspect, here disregarded, has been taken into account, for instance, by Mariani et al. [26].

3. Proposed algorithm

If a traditional finite element analysis is performed to simulate the mechanical response of polycrystalline solids under impact dynamics and crack propagation, as described in Section 2, the resulting computational burden can be very high, especially if a fully three-dimensional problem is addressed. In fact, a very refined mesh is required to properly describe the grain boundaries and to resolve the cohesive zone length; on the one hand, this leads to an high number of degrees of freedom, on the other hand, if an explicit integration scheme is adopted, a very small explicit time step is needed to fulfil the Courant–Friedrichs–Lewy condition and correctly reproduce the elastic wave propagation. The high computational burden of a three-dimensional simulation remains the major drawback, even if an implicit/explicit algorithm is considered, as in [1,2,26,34,35], adopting an unconditionally stable implicit integration scheme during the elastic phase and switching to an explicit rule at the crack onset.

A domain decomposition technique is proposed in this work to overcome this limitation and to readdress the fracture propagation problem in a continuum. The starting point has been the dual Schur's domain decomposition method, developed by Gravouil and Combescure [3] for the solution of the structural dynamic problem, that allows for the coupling of different time integration schemes of the Newmark's family and different time scales. The procedure introduced in [3] has been here extended to the numerical simulation of fracture phenomena, with the particular application to heterogeneous polycrystalline materials, like polysilicon. The main idea is to couple a domain decomposition framework to an implicit–explicit integration scheme: only the subdomains loci of fracture propagation have to switch to an explicit time scheme, while an unconditionally stable implicit scheme is associated to the others. In principle, the present formulation allows to assign a different time scale to each subdomain. However, only two time scales have been considered here, associated respectively with the implicit time step and the explicit one. For the sake of simplicity, the implicit time step is assumed as an integer multiple of the explicit one, computed on the basis of the Courant–Friedrichs–Lewy condition.

The hypotheses at the basis of the developed techniques are:

1. matching meshes at the interface between subdomains;
2. same finite element formulation for all subdomains;
3. explicit integration scheme for the non linear subdomains.

The first two assumptions allow to guarantee that the numerical dissipation due to the introduction of the domain decomposition approach, basically linked to the work of the interface forces, does not sensibly affects the energy

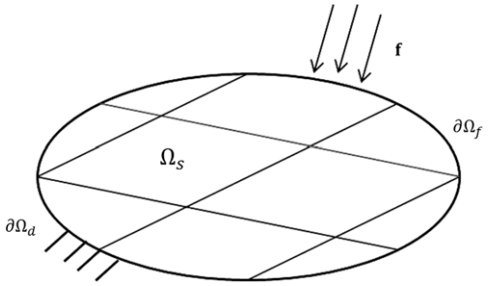

Fig. 4. Partition into subdomains.

balance of the system and remains small if compared with the fracture energy [4,36–39]. The third condition allows to predict without any iteration the displacement at the end of each time step and, consequently, the displacement jump at each cohesive element. As far as all the subdomains remain linear elastic, the original algorithm developed by Gravouil and Combescure [3] applies. When a crack starts to propagate, the procedure has to be modified and three different cases have been considered: fracture propagating inside a subdomain, along the connectivity interface (i.e. the interface between subdomains), and across it. The proposed domain decomposition algorithm has been implemented in a three dimensional finite element code. Ten nodes tetrahedra are used for the bulk, while six nodes triangles are employed as interface elements. The implemented code has been weakly parallelized, using the Open Multi-Processing (OpenMP) directives as parallel programming tool in a shared memory architecture. The parallel performance is not yet satisfactory. The main reason lies in the multi-time-step nature of the proposed algorithm: it affects the load-balancing of the parallel computations so that, when fracture occurs, only the explicit subdomains are solved at each time instant, and the cores associated to the implicit ones are activated only at the end of the coarse time steps.

3.1. Initial elastic phase

In this initial phase, the proposed algorithm works as the domain decomposition technique for the dynamic mechanical problem formulated by Gravouil and Combescure [3], here briefly resumed. Let us introduce a decomposition into N_s non-overlapping subdomains Ω_s with $s = 1, \ldots, N_s$, as shown in Fig. 4. Each subdomain can be seen as an independent body, subjected both to external and to interface forces, such that the continuity of the whole domain is restored.

Considering, for the sake of simplicity, the case of linear elasticity under the hypothesis of small deformation and displacements, the local equilibrium of each subdomain Ω_s can be written as:

$$\mathbf{M_s}\ddot{\mathbf{U}}_\mathbf{s} + \mathbf{K_s}\mathbf{U}_s = \mathbf{F}_s^{ext} + \mathbf{B}_\mathbf{s}^T\boldsymbol{\Lambda} \quad \text{for } s = 1, \ldots, N_s \tag{12}$$

where $\mathbf{M_s}$, $\mathbf{K_s}$, $\ddot{\mathbf{U}}_\mathbf{s}$, $\mathbf{U_s}$, $\mathbf{F_s}$ represent the mass matrix, the stiffness matrix, the acceleration vector, the displacement vector and the nodal force vector of subdomain s respectively; $\mathbf{B_s}$ is a signed Boolean connectivity matrix, which links the degrees of freedom of the whole subdomain to those belonging to the connectivity interface between subdomains. A Lagrange multiplier approach is adopted to deal with the partitioned domain and enforce the continuity between subdomains: $\boldsymbol{\Lambda}$ is a vector of Lagrange multipliers, whose physical meaning is that of interface forces, exchanged by each subdomain with the surrounding ones through the interfaces.

Moreover, an additional equation, expressing the kinematic constraint at the interface, has to be introduced. As usual for a dual approach, equilibrium of interface forces is assumed *a priori*, while compatibility has to be explicitly enforced. In discretized dynamics, continuity at the interface should be, in principle, prescribed in terms of only one field to choose among displacements, velocities or accelerations. Gravouil and Combescure [3] proved that expressing the compatibility condition in terms of the velocity leads to a stable algorithm, even when arbitrary integration schemes and different time scales are coupled. Thus, the following condition is enforced:

$$\sum_{s=1}^{N_s} \mathbf{B_s}\dot{\mathbf{U}}_\mathbf{s} = \mathbf{0}. \tag{13}$$

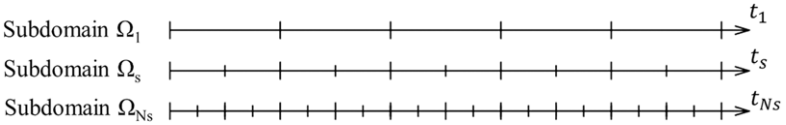

Fig. 5. Example of different time scales.

The algorithm is multi-time-step: each subdomain is characterized by its own time step Δt_s and integration scheme with the only assumption that all the time steps are integer multiples of the reference one, as shown in Fig. 5. Introducing time discretization, indicating with n_{s+1} the current time instant of subdomain Ω_s, and integrating by means of Newmark's scheme, Eq. (12) becomes:

$$\tilde{\mathbf{M}}_{\mathbf{s}}\ddot{\mathbf{U}}_{s_{n_s+1}} = \mathbf{F}^{ext}_{s_{j_s+1}} - \mathbf{K}^{p}_{\mathbf{s}}\mathbf{U}_{s_{n_s}} + \mathbf{B}^{T}_{\mathbf{s}}\boldsymbol{\Lambda}_{s_{j_s+1}} \quad \text{for } s = 1, \ldots, N_s \tag{14}$$

with:

$$\tilde{\mathbf{M}}_{\mathbf{s}} = \mathbf{M}_{\mathbf{s}} + \beta_s \Delta t_s^2 \mathbf{K}_s \tag{15a}$$

$$\mathbf{U}_{s_{n+1_s}} = {}^{p}\mathbf{U}_{s_{n_s}} + \beta_s \Delta t_s^2 \ddot{\mathbf{U}}_{s_{n+1_s}} \tag{15b}$$

$$\dot{\mathbf{U}}_{s_{n+1_s}} = {}^{p}\dot{\mathbf{U}}_{s_{n_s}} + \gamma_s \Delta t_s \ddot{\mathbf{U}}_{s_{n+1_s}} \tag{15c}$$

$${}^{p}\mathbf{U}_{s_{n_s}} = \mathbf{U}_{s_{n_s}} + \Delta t_s \dot{\mathbf{U}}_{s_{n_s}} + \frac{1}{2}(1-\beta_s)\Delta t_s^2 \ddot{\mathbf{U}}_{s_{n_s}} \tag{15d}$$

$${}^{p}\dot{\mathbf{U}}_{s_{n_s}} = \dot{\mathbf{U}}_{s_{n_s}} + (1-\gamma_s)\Delta t_s \ddot{\mathbf{U}}_{s_{n_s}} \tag{15e}$$

being β_s and γ_s the parameters of the integration scheme adopted for subdomain Ω_s. In the numerical examples here proposed, γ_s has been always considered equal to 0.5, while β_s has been taken equal to 0.25 for the implicit integration scheme and to 0 for the explicit one.

The basic idea of the algorithm proposed by Gravouil and Combescure [3] is to split the solution of Eq. (14) into two contributions, respectively denoted as *unconstrained* and *constrained problem*. The *unconstrained* or *free problem* considers the free motion of each unconnected subdomain, under the effect of the external loads and of displacements or velocities imposed at the Dirichlet boundary $\partial\Omega_d$. The *constrained* or *link problem* evaluates the correction to the previous solution, computing the interface forces to be applied to each subdomain to re-glue it to the others. The global solution can thus be obtained as the superposition of the solutions of an *unconstrained problem* and of a *constrained problem*, in the following respectively marked with the superscripts *free* and *link*.

$$\tilde{\mathbf{M}}_{\mathbf{s}}\ddot{\mathbf{U}}^{free}_{s_{n_s+1}} = \mathbf{F}^{ext}_{s_{n_s+1}} - \mathbf{K}^{p}_{\mathbf{s}}\mathbf{U}_{s_{n_s}} \tag{16a}$$

$$\tilde{\mathbf{M}}_{\mathbf{s}}\ddot{\mathbf{U}}^{link}_{s_{n_s+1}} = \mathbf{B}^{T}_{\mathbf{s}}\boldsymbol{\Lambda}_{n_s+1} \quad s = 1, \ldots, N_s. \tag{16b}$$

The kinematic fields of the global domain are given by the superposition of the solution of these two problems, as follows:

$$\mathbf{U}_{s_{n_s+1}} = \mathbf{U}^{free}_{s_{n_s+1}} + \mathbf{U}^{link}_{s_{n_s+1}} \tag{17a}$$

$$\dot{\mathbf{U}}_{s_{n_s+1}} = \dot{\mathbf{U}}^{free}_{s_{n_s+1}} + \dot{\mathbf{U}}^{link}_{s_{n_s+1}} \tag{17b}$$

$$\ddot{\mathbf{U}}_{s_{n_s+1}} = \ddot{\mathbf{U}}^{free}_{s_{n_s+1}} + \ddot{\mathbf{U}}^{link}_{s_{n_s+1}}. \tag{17c}$$

The system of equations (13) and (16b) leads to the following condensed interface problem, written at the generic time step of the reference scale:

$$\mathbf{H}\boldsymbol{\Lambda}_{n+1} = -\sum_{s=1}^{N_s} \mathbf{B}_{\mathbf{s}}\dot{\mathbf{U}}^{free}_{s_{n+1}} \tag{18}$$

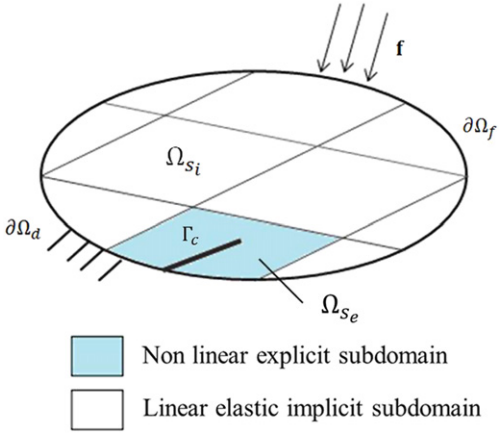

Fig. 6. Crack propagation inside a subdomain.

being $\mathbf{H}$ the interface operator, defined as:

$$\mathbf{H} = \sum_{s=1}^{N_s} \gamma_s \Delta t_s \mathbf{B_s} \tilde{\mathbf{M}}_\mathbf{s}^{-1} \mathbf{B}_\mathbf{s}^T = \sum_{s=1}^{N_s} \mathbf{H_s}. \tag{19}$$

The computation of the *free* velocity of subdomain Ω_s at time $n+1$ of the reference time scale is handled by linear interpolation over the corresponding time step of subdomain Ω_s. Note that the computational burden related to the calculation of $\mathbf{H_s}$ is higher for the implicit subdomains than for the explicit ones. For the implicit subdomains, it is indeed required to determine the columns of the inverse of the equivalent mass matrix $\tilde{\mathbf{M}}_\mathbf{s}$ corresponding to the degrees of freedom belonging to the subdomain's interface, while for the explicit subdomains this computation can be avoided, since the mass matrix is diagonal. Anyway, given that only the elastic subdomains are integrated implicitly, the computation of $\mathbf{H_s}$ for each implicit subdomain has to be performed just once during the analysis. For the implicit or the implicit–explicit computations, it would be an interesting development to introduce an iterative solver for the interface and the link problems, as usually done for the FETI method. This approach would be more suitable for a parallel solution, especially if the preconditioners developed for the FETI method (see, for instance, [10,40–42]) are exploited in order to avoid the direct assemble of the interface operator and to perform only subdomain-by-subdomain calculations.

As far as all the subdomains remain linear elastic, an implicit reference time scale is defined and all the subdomains are synchronous with it. Since there is no need to handle multiple time scales in this initial phase, the general formulation of the algorithm can be simplified, considering the same time step for all the subdomains. As a consequence, at the generic time step $[t_n - t_{n+1}]$, the mechanical response of each subdomain is governed by:

$$\mathbf{M}_{s_{n+1}} \ddot{\mathbf{U}}_{s_{n+1}} + \mathbf{K}_s \mathbf{U}_{s_{n+1}} = \mathbf{F}^{ext}_{s_{n+1}} + \mathbf{B}_s^\mathbf{T} \mathbf{\Lambda}_{n+1} \quad s = 1, \ldots, N_s. \tag{20}$$

Also, the *free* and *link* problem of subdomain Ω_s can be written in a simpler form as:

$$\tilde{\mathbf{M}}_s \ddot{\mathbf{U}}^{free}_{s_{n+1}} = \mathbf{F}^{ext}_{s_{n+1}} - \mathbf{K}_s^p \mathbf{U}_{s_n} \tag{21}$$

$$\tilde{\mathbf{M}}_s \ddot{\mathbf{U}}^{link}_{s_{n+1}} = \mathbf{B}_s^\mathbf{T} \mathbf{\Lambda}_{n+1} \quad s = 1, \ldots, N_s. \tag{22}$$

At each implicit time step, it is possible to reconstruct the displacement, velocity and acceleration fields over the whole domain. The fracture activation test can be thus carried out on all the elements' faces, similarly to the monolithic case, described in Section 2.

3.2. Fracture propagating inside a subdomain

As long as the fracture develops inside a single subdomain, such as schematically represented in Fig. 6, only the cracked subdomain switches to an explicit scheme, while the others keep the implicit scheme.

Moreover, at fracture initiation, the fine, explicit time scale becomes the reference one: this means that the non linear subdomains are synchronous with it, while the elastic ones are integrated with a coarse time step. The algorithm is now fully multi-time-step and two time scales are present. The equations are hereinafter written with reference to a generic time step of the coarse implicit time scale $[t_n - t_{n+1}]$, with $t_{n+\frac{j+1}{m}}$ $(j \in [0, m-1])$ denoting an intermediate time instant of the fine scale.

As pointed out by Pandolfi and Ortiz [43], Pandolfi and Ortiz [44], Celes et al. [45], Paulino et al. [46], the geometrical topology has to be adaptively updated to take into account the insertion of new cohesive elements. To handle the crack propagation in the subdomain, cohesive elements are indeed inserted run-time: whereas an activation criterion is satisfied, the corresponding faces have to be duplicated to allow for the creation of a new cohesive element. At the beginning, the new face and the original one share all the nodes and the edges, while the crack opening is allowed, progressively duplicating and releasing the nodes and the edges. Consequently, the subdomains data structure has to be modified on-the-fly, updating the list of nodes belonging to the subdomain itself, while the element list remains the same during the whole analysis. Also the topology data structure has to be changed. When a node is duplicated to allow for crack opening, the degrees of freedom of the new node inherit the displacements, the velocities and the accelerations of those of the original node as initial conditions. Moreover, the mass matrix of the cracked subdomain has to be recomputed with the updated connectivity, so that there are no jumps in the strain and in the kinetic energies of the system.

Eq. (20) still holds for all the elastic subdomains, while both a term of internal forces and of cohesive forces has to be considered for the non linear subdomains. In the case of fracture processes, the internal force vector is indeed given by an elastic term related to the bulk material of the subdomain $\Omega_{s_e} \backslash \Gamma_c$, while the cohesive forces vector $\mathbf{F}^{coh\,sub}$ derives from the cohesive elements inserted in the subdomain:

$$\mathbf{F}^{int}_{s_e} = \mathbf{K}_{s_e} \mathbf{U}_{s_e}. \tag{23}$$

As a consequence of the explicit integration rule, those terms depend only on the predictor of displacement and not on the solution at the end of the time step. Thus, the mechanical behaviour of a cracked subdomain is described by:

$$\mathbf{M}_s \ddot{\mathbf{U}}_{s_e} + \mathbf{F}^{int}_{s_e}({}^p\mathbf{U}_{s_e}) + \mathbf{F}^{coh\,sub}({}^p\mathbf{U}_{s_e}) = \mathbf{F}^{ext}_{s_e} + \mathbf{B}^{\mathbf{T}}_s \mathbf{\Lambda}. \tag{24}$$

Denoting with the subscript s_e the generic explicit subdomain and with s_i an implicit one, the *free* and *link* problems for the implicit and the explicit subdomains can be written at the coarse time instant t_{n+1} and at the fine time instant $t_{n+\frac{j+1}{m}}$ (being m the integer ratio between the implicit and the explicit time step) respectively as:

Implicit elastic subdomains

Free problem for the elastic implicit subdomains

$$\tilde{\mathbf{M}}_{s_i} \ddot{\mathbf{U}}^{free}_{s_{i_{n+1}}} = \mathbf{F}^{ext}_{s_{i_{n+1}}} - \mathbf{K}^{p}_{s_i} \mathbf{U}_{s_{i_n}}. \tag{25}$$

Link problem for the elastic implicit subdomains

$$\tilde{\mathbf{M}}_{s_i} \ddot{\mathbf{U}}^{link}_{s_{i_{n+1}}} = \mathbf{B}^{\mathbf{T}}_{s_i} \mathbf{\Lambda}_{n+1}. \tag{26}$$

Non linear explicit subdomains

Free problem for the non linear explicit subdomains

$$\mathbf{M}_{s_e} \ddot{\mathbf{U}}^{free}_{s_e\,n+\frac{j+1}{m}} = \mathbf{F}^{ext}_{s_e\,n+\frac{j+1}{m}} - \mathbf{F}^{int}_{s_e\,n+\frac{j+1}{m}}({}^p\mathbf{U}_{s_e\,n+\frac{j}{m}}) - \mathbf{F}^{coh\,sub}_{s_e\,n+\frac{j+1}{m}}({}^p\mathbf{U}_{s_e\,n+\frac{j}{m}}). \tag{27}$$

Link problem for the non linear explicit subdomains

$$\mathbf{M}_{s_\mathbf{e}} \ddot{\mathbf{U}}^{link}_{s_e\,n+\frac{j+1}{m}} = \mathbf{B}^{\mathbf{T}}_{s_i} \mathbf{\Lambda}_{n+\frac{j+1}{m}}. \tag{28}$$

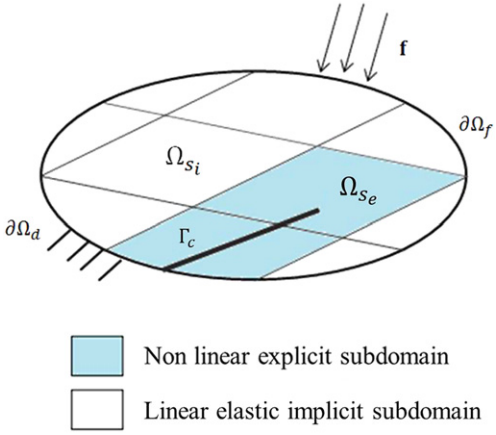

Fig. 7. Crack propagation across the connectivity interface between subdomains.

Whenever a cohesive element has been inserted at the previous time step or the nodes of an existing interface element have been duplicated, the mass matrix of the explicit subdomain Ω_{s_e} has to be computed again, to take into account the change in the topology and, consequently, in the degrees of freedom of the subdomain.

As long as the cracks do not reach the connectivity interface, the continuity between subdomains is restored imposing an interface condition written in terms of velocities. Although the formulation of the interface problem and of the *link* one is not affected by the presence of fractures that remain internal to a single subdomain, the global interface operator $\mathbf{H}$ has to be re-assembled at any change in the mass matrix of the explicit subdomain. Basically, only the local contribution $\mathbf{H}_{\mathbf{s_e}} = \gamma_{s_e} \Delta t_{s_e} \mathbf{B}_{\mathbf{s_e}} \mathbf{M}_{\mathbf{s_e}}^{-1} \mathbf{B}_{\mathbf{s_e}}^T$ of the explicit subdomain Ω_{s_e} has to be recomputed, whenever a fracture has propagated in the previous time step, while the matrices $\mathbf{H}_{\mathbf{s_i}}$ of the implicit subdomains are stored. It is worth noting that the computation of $\mathbf{H}_{\mathbf{s_e}}$ is not particularly burdensome, since a lumped mass matrix is considered.

3.3. Fracture propagating across the interface between subdomains

The case of a crack intersecting the connectivity interface between subdomains, as shown in Fig. 7, occurs if the activation test is met on a face internal to a subdomain, but with an edge belonging to the connectivity interface. The cohesive element insertion and the node duplication, thus, changes the number of nodes belonging to the connectivity interface. Basically, the interface nodes belonging to the opened edge, on one hand have a different local numeration on each subdomain, on the other hand are duplicated, as usual, to allow for a crack crossing the connectivity interface. Let us consider, for instance, the midnode n of the cracked edge and denote with n_i and n_j, and with n_i' and n_j' the local numerations of the original node n and of its duplicate n', seen as belonging to subdomain Ω_i or Ω_j respectively. Interface forces are applied between n_i' and n_j' to restore the continuity between subdomains Ω_i and Ω_j, while cohesive forces act between n_i and n_i' and between n_j and n_j', as shown in Fig. 8.

Both subdomains at the two sides of the crack switch to an explicit time step, so that they become synchronous and no interpolation is introduced in predicting the displacement jump at the interface. The formulation of the *free* and of the *link problems* for the implicit subdomains and for the explicit ones remains the same previously recalled. At difference with the case of a crack propagating on a single subdomain, the fracture propagation requires to update not only the subdomains data structure, but also the connectivity interface one, modifying the list of nodes belonging to them.

3.4. Fracture propagating along the interface between subdomains

When a fracture is propagating along the interface between subdomains, like in Fig. 9, the fracture activation test is satisfied on faces lying on the connectivity interface and the two sides of the crack naturally coincide with faces belonging to two different subdomains. As usual, the original face is duplicated and a cohesive element is introduced between the two faces, then progressively duplicating also the edges and the nodes. All the original geometrical entities are associated to one subdomain, while the duplicated ones to the other. The connectivity interface between

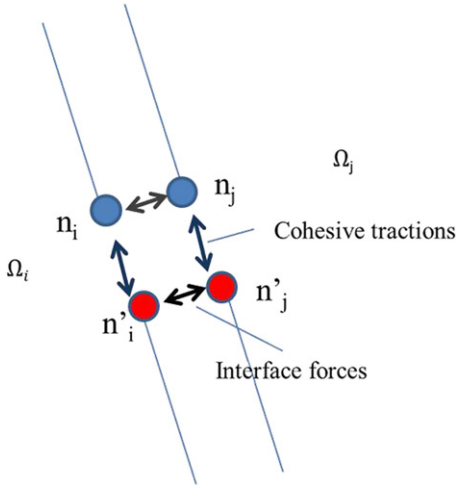

Fig. 8. Fracture crossing the connectivity interface between subdomains: duplication of nodes.

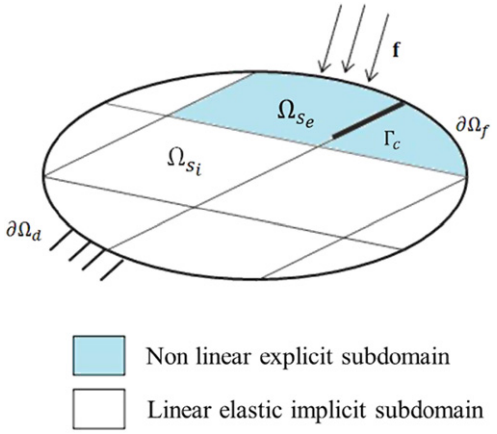

Fig. 9. Crack propagation along the connectivity interface between subdomains.

subdomains is therefore partitioned into two portions: the first, where the continuity is still imposed, and the second, where the crack is opening and the cohesive elements are inserted. As a result, the interface operator $\mathbf{H}$ has to be re-assembled at every change in the interface topology, recomputing the interested matrices $\mathbf{H_s}$ on a reduced set of interface's degrees of freedom, corresponding to the nodes where the continuity is still imposed. Formally, this can be written by updating the connectivity matrices $\mathbf{B_s}$ to the current topology of the interface. The tractions deriving from the integration of the constitutive, softening law are locally imposed as interface forces for the subdomains, so an internal force term related to the presence of the cohesive elements has indeed to be added to the right hand side of the *link* problem, to take into account for the presence of the cohesive tractions acting at the interface. Both the subdomains separated by the cracked connectivity interface switch to an explicit time integration.

Adopting an explicit integration rule for both the subdomains, the discontinuity at the interface can be predicted without any iteration, since it is a function only of the solution at the beginning of the time step. The *free* and *link problems* for the implicit and explicit subdomains can be written at the coarse time instant t_{n+1} and at the fine time instant t_{j+1} respectively as:

Implicit elastic subdomains

Free problem for the elastic implicit subdomains

$$\tilde{\mathbf{M}}_{s_i}\ddot{\mathbf{U}}^{free}_{s_{i_{n+1}}} = \mathbf{F}^{ext}_{s_{i_{n+1}}} - \mathbf{K}^{p}_{s_i}\mathbf{U}_{s_{i_n}}. \tag{29}$$

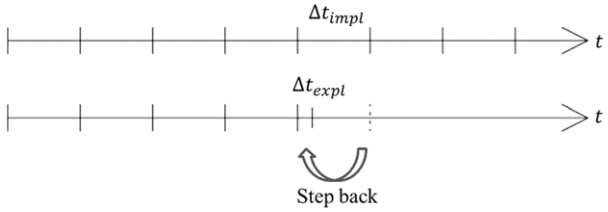

Fig. 10. Step back.

Link problem for the elastic implicit subdomains

$$\tilde{\mathbf{M}}_{s_i} \ddot{\mathbf{U}}^{link}_{s_{i_{n+1}}} = \mathbf{B}^{\mathbf{T}}_{s_i} \mathbf{\Lambda}_{n+1}. \tag{30}$$

Non linear explicit subdomains

Free problem for the non linear explicit subdomains

$$\mathbf{M}_{s_e} \ddot{\mathbf{U}}^{free}_{s_{e_{j+1}}} = \mathbf{F}^{ext}_{s_{e_{j+1}}}. \tag{31}$$

Link problem for the non linear explicit subdomains

$$\mathbf{M}_{s_e} \ddot{\mathbf{U}}^{link}_{s_{e_{j+1}}} = \mathbf{B}^{\mathbf{T}}_{s_i} \mathbf{\Lambda}_{j+1} - \mathbf{F}^{coh\,int}_{s_{e_{j+1}}}({}^{p}\mathbf{U}_{s_{e_j}}). \tag{32}$$

An alternative solution, here not exploited, would be to consider the crack propagating along the interface as belonging to either subdomain facing the crack, basically reducing to the case of a crack propagating inside a subdomain. The cohesive forces will, thus, appear as internal forces for the chosen subdomain, while the link problem would remain formally equal to Eq. (28), except that both the subdomains facing the interface crack would switch to an explicit time integration. This second solution could be interesting if a real parallelization of the code is addressed. The updating of the degrees of freedom belonging to the interface between subdomains could be indeed avoided. Moreover, it would be possible to perform the modification of the topology and the computation of the cohesive forces at the local level of the cracked subdomain, without involving the interface problem, which requires to exchange data between the subdomains.

In the formulation of the interface problem special attention should be paid to the handling of the so-called cross-points, which are points shared by more than two subdomains. In the three dimensional case, the cross-point becomes, in general, a cross-edge. In the present work, a non-redundant formulation has been employed for the cross-points, where the interface continuity has to be imposed. An *ad hoc* procedure for the construction of the connectivity in correspondence to the cross-points is thus employed in order to correctly write the kinematic constraint and avoid redundancies in the description of the interface.

3.5. Time scales handling

As already pointed out, as long as all the subdomains remain linear elastic, an implicit reference time scale is defined and all the subdomains are synchronous with it. When the first crack initiates, the reference time scale becomes the explicit one and the algorithm turns effectively multi-time-scale. The velocity fields of the elastic subdomains are exactly computed at the implicit time instants of the coarse scale only; they are linearly interpolated in order to evaluate the right hand side of the interface problem, since continuity at the interface is imposed at each intermediate instant of the finer explicit time scale. The change in the reference time scale is carried out through a step back to the previous implicit time instant for all the subdomains, as shown in Fig. 10.

Thereafter, every time a subdomain becomes explicit, a step back to the last computed implicit time instant should, in principle, be performed only for that subdomain, while only the *link problem* should be re-computed for the others. This is, for instance, the case of a crack coming from a subdomain and then propagating to another. This further step back to the last implicit time instant would require to store the *free* solution vectors for a possibly high number of

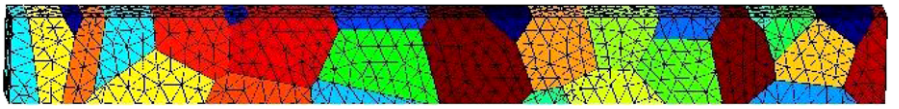

Fig. 11. Example of grain morphology.

Fig. 12. Example of geometrical decomposition of the domain: grid partitioning.

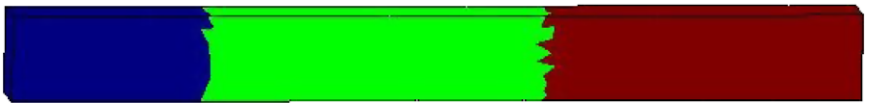

Fig. 13. Example of geometrical decomposition of the domain: slices partitioning.

explicit time steps. To avoid this procedure, two strategies have been implemented. Basically, the complete solution for all the subdomains is stored only at each instant of the implicit time scale, when it has been completely reconstructed. Moreover, at those time instants an activation test is performed on the elastic subdomains. If an elastic subdomain fulfils the fracture test, it switches to the explicit time integration and a step back to the last implicit time step is performed for all the subdomains, adopting the last stored solution as initial conditions. On the other hand, if the fracture criterion is not met, the maximum of the effective scalar tractions computed for each subdomain is compared with the critical stress threshold multiplied by a safety factor $\alpha < 1$ (usually it has been considered $\alpha = 0.8$). If this value is exceeded, the subdomain switches to an explicit time scheme, even if no cohesive elements are inserted. In this way, it could be avoided to recompute the solution for the m explicit time steps sub-dividing the implicit time step.

The change in the time step is a cumbersome issue, since it could cause instability in the time integration, especially if the ratio m between the implicit and explicit time steps is high. Up to now, a posteriori check is carried out by verifying that the error in the energy balance does not exceed a suitable threshold. If this test is not met, the implicit time step is reduced and a new step back to the initial time instant of the implicit time step is performed.

4. Partitioning techniques

Different mesh partition strategies have been considered in this work, graphically illustrated by subdividing the unstructured mesh of a prismatic polycrystalline solid, shown in Fig. 11.

The first one is a simple geometrical partition: the analysis domain is cut by means of a regular grid or into slices. In the former case, three input parameters, namely the values of the grid's step in the three spatial directions, are necessary to determine the mesh subdivision, while, in the latter case only the distance between the slices is required. An element partitioning is performed: each element is assigned to a subdomain if its centroid belongs to a cell of the grid or to a slice. Figs. 12 and 13 show an example of grid and slices partitioning respectively.

A second technique exploits the automatic decomposer algorithm developed by Farhat in [47]; subdomains are created in order to balance the number of elements and optimize the partition for parallel computation; an example is given in Fig. 14. As pointed out by Vanderstraeten and Keunings [48], the goals of an optimal partitioning of an unstructured mesh should ideally be both to reach the computational load balancing between subdomains and to minimize the global size of the interface between them. The load balancing is determined by the number of elements per subdomain only if the computation is completely explicit. In the case of implicit time stepping, other factors, such as the bandwidth of the stiffness matrix, influence the overall performance of the parallelism, but cannot be evaluated a priori. For this reason, if all the subdomains are synchronous, the load balancing could be assumed roughly satisfied, whereas the number of elements per subdomain is as close as possible to the ratio $\frac{N_e}{N_s}$, being N_e the total number of elements of the mesh and N_s the number of subdomains. This assumption is satisfied by the Finite Element Tearing and

Fig. 14. Example of automatic partitioning of the domain.

Fig. 15. Example of grain partitioning of the domain.

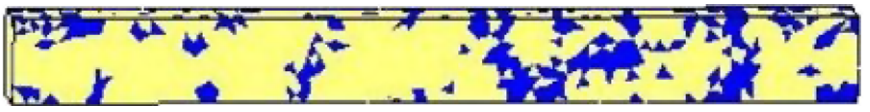

Fig. 16. Example of partitioning of the domain by element size.

Interconnecting Method, with respect to which the decomposer technique has been written, but not by the proposed multi-time-step algorithm: when fracture is propagating, the solution is performed at each time step for the explicit non linear subdomains only; this of course affects the computational gain.

A third partitioning strategy is naturally suggested by the grain structure of polycrystalline materials: subdomains are conceived as a set of one or more grains, as shown in the example of Fig. 15.

Finally, a fourth partition procedure has been developed, which divides the elements on the basis of their size, as depicted in Fig. 16. To accurately model the grain morphology, in fact, refined meshes with some elements of very small size are typically required. As it has been already pointed out, this need penalizes considerably the computational cost, since it leads to very small time steps, due to the Courant–Lewy–Friedrichs condition. Therefore, in this partition technique basically only two subdomains are created: the first containing the "small" elements, i.e. the elements whose size is lower than a critical value, and the second one composed by the "large" elements. A spatial partitioning technique, that generalizes the explicit central-difference time integration scheme to the case of spatially variable time step, has been already proposed by Casadei and Halleux [49], although these authors did not integrate this technique into a domain decomposition algorithm. The elements' size is evaluated computing the minimum distance between the centroid of the tetrahedron and its vertices. At difference with the other partitioning techniques, two explicit time scales, a coarse one for the subdomain with the large elements and a fine one for the other subdomain, are in this case required.

5. Numerical examples

To show the efficiency of the proposed method, four numerical examples are presented in this section.

First, we check the quality of our solution and the correctness of the implementation by comparing our approach with well-known analytic and/or numerical benchmarks, namely an (alumina) double cantilever beam (studied, e.g., in [50–52]) and Kalthoff's experiment [53]. In the last two examples, we show typical polysilicon MEMS details under dynamic load, as a paradigmatic problem in the industrial context of microsystems.

Moreover, while the stability of the domain decomposition approach has been stated in [3] and we do not provide a formal proof when a fracture propagates (but some work has been done on the topic, see, e.g. [54] and references therein), we are however confident that the energy balances reported in all the following calculations give credit to the assumption of stability for the algorithm. In particular, we show that, in all the cases, the numerical dissipation, introduced by the solution of the interface problem between the subdomains, remains negligible with respect to the total energy in the system.

The results of the proposed domain decomposition technique are compared with those deriving from a monolithic finite element simulation performed with an implicit–explicit algorithm, as in [1] and in [34]: the integration scheme is implicit until the fracture onset, then it switches to explicit for the overall domain.

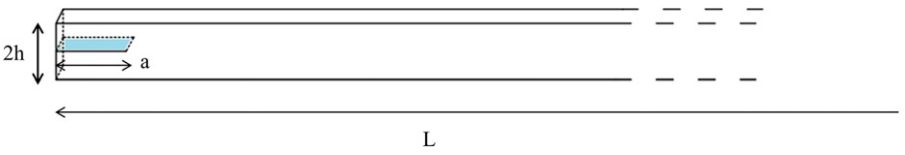

Fig. 17. Double cantilever beam geometry.

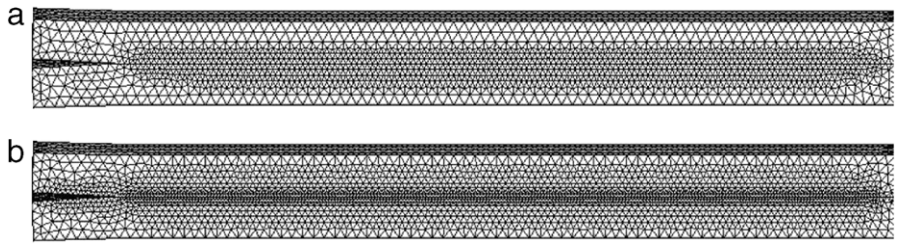

Fig. 18. Finite element discretizations: (a) coarse mesh, (b) fine mesh.

Table 1
Double cantilever beam test. Partition into subdomains: number of nodes and elements per subdomain.

Subdomain	Number of elements	Number of nodes
Ω_1	25,065	37,065
Ω_2	28,648	42,535
Ω_3	2,226	4,193
Ω_4	1,957	3,716

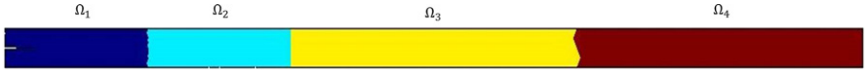

Fig. 19. Partition into subdomains.

5.1. Double cantilever beam

As a first example, a double cantilever beam test [50–52] is considered. The specimen geometry, shown in Fig. 17, and the material properties are those proposed in [27]. In detail, the beam length L is taken equal to 4 mm, but the analysis domain has been extended up to 12 mm, so that the crack propagation is not influenced by the wave reflections from the right end of the beam; anyway, fracture is allowed to propagate in the first part of the domain only. The beam has a rectangular cross section whose width B is equal to 0.1 mm and the height $2H$ is equal to 0.2 mm. The initial crack length a is taken equal to 0.4 mm. The material is alumina, characterized by isotropic mechanical properties, with Young's modulus $E = 260$ GPa, Poisson's coefficient $\nu = 0.21$ and mass density $\rho = 3690\ \frac{\text{kg}}{\text{m}^3}$. The cohesive law is determined by a maximum tensile strength $\sigma_{\max} = 400$ MPa and fracture energy $G_c = 34\ \frac{\text{N}}{\text{m}}$.

Two different unstructured finite element discretizations have been considered: a coarse and a fine mesh, characterized by an element size respectively equal to 25 μm and to 15 μm along the beam axis, where the crack is expected to propagate. In both cases the discretization becomes, conversely, less refined near the upper and the bottom side of the beam and in the elastic part on the right. Both choices of the element size resolve the cohesive zone length $l_c = \frac{E\, G_c}{(t_{\max})^2} = 55$ μm. The coarse mesh is characterized by 57,896 quadratic tetrahedral elements and 86,936 nodes, while the fine one comprises 268,782 quadratic tetrahedral elements and 193,843 nodes. The obtained finite element meshes are shown in Fig. 18.

The domain has been partitioned into four subdomains, two in the left part and two in the right one, as shown in Fig. 19. Table 1 gives the number of nodes and elements of each subdomain.

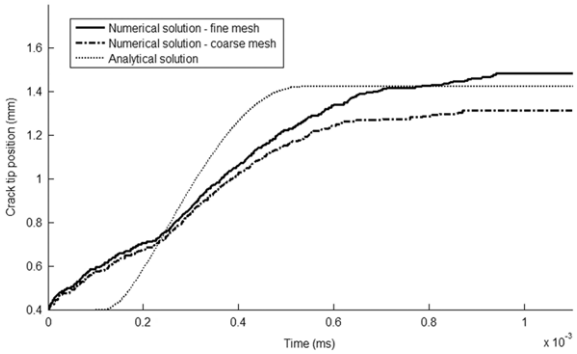

Fig. 20. Double cantilever beam test. Crack tip position: $W_0 = 0.4$ μm.

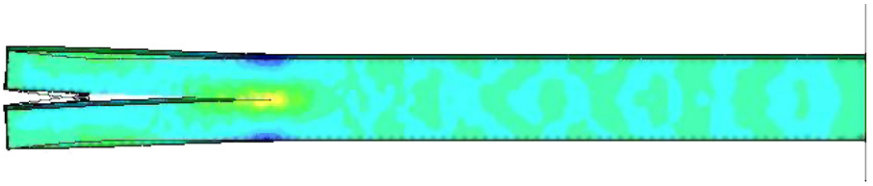

Fig. 21. Double cantilever beam test. Deformed shape: $W_0 = 0.4$ μm.

The DCB test is carried out by imposing wedge loads (i.e. vertical and opposite loads) at the pins; when the crack starts to propagate the load is kept constant, until the crack arrests. The initial conditions at the crack propagation inception are here reproduced, performing a static elastic analysis under an imposed crack tip opening displacement W_0 without allowing for crack propagation. Then, the crack is allowed to propagate from the tip to the bulk of the specimen. Two cases have been considered: $W_0 = 0.4$ μm and $W_0 = 1.2$ μm.

5.1.1. Small imposed crack opening displacement

Fig. 20 shows the crack tip position histories for the small crack opening displacement case, obtained with the two considered meshes. Two different stages can be identified: in the first one, roughly until 0.2 ms, the crack propagation is governed by the stress wave propagation, while in the second one it is determined by a beam-like behaviour. Finally, the crack arrests at about 0.6 ms. The numerical results have been compared with the analytical solution developed in [52], where use has been made of the Bernoulli–Euler beam theory, modelling the upper and the lower arms, as beams of evolving length.

A good agreement can be observed between the analytical and the numerical results, even if some discrepancies can be detected in the first part of the curve, due to the fact that the analytical solution is not able to describe the effect of the elastic waves on the crack propagation. Moreover, it can be noticed that the obtained final crack length agrees with the analytical estimation.

The final deformed shape is shown in Fig. 21. Notice that the displacements have been magnified by a factor equal to 10. Crack propagates only inside subdomain Ω_1, without reaching the connectivity interface. As a consequence, the interface operator has to be re-computed only once to take into account the change in the integration scheme of subdomain Ω_1: considering the case of the coarse mesh, its condition number is initially equal to 22.23, then it becomes 27.45, when crack starts to propagate.

Fig. 22 shows the energy balance. It is worthwhile to emphasize that the introduction of a domain decomposition approach causes a minimal dissipation, on the order of 1% of the global energy balance.

Table 2 gives the analysis times and the computational gain. The proposed numerical procedure allows for a reduction respectively of the 40% of the total analysis time with respect to a standard monolithic finite element simulation.

Table 3 reports the analysis times required by each phase of the analysis, namely, the solution of the *free problem* (including the matrices assemble), the solution of the interface and of the *link* problems, the post-processing phase (i.e. the reconstruction of the overall solution and the stress recovery) and the fracture handling.

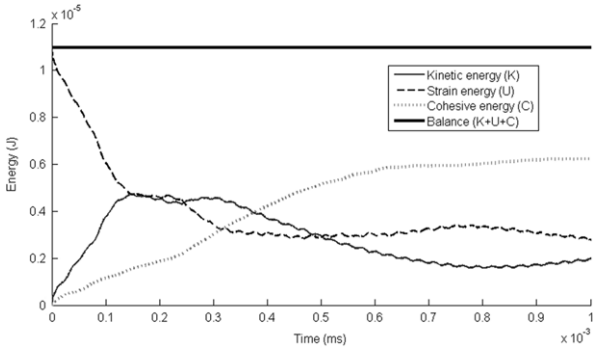

Fig. 22. Double cantilever beam test. Energy balance: $W_0 = 0.4$ μm.

Table 2
Double cantilever beam—small imposed crack opening displacement: analysis times and computational gain (calculations were carried out on an Intel Core i7-870 Cpu@2.93 GHz).

Algorithm	Analysis time (h)	Computational gain
Monolithic analysis	25	–
Domain decomposition	15	40%

Table 3
Double cantilever beam—small imposed crack opening displacement: detailed spent times.

Phase	Spent time (h)	Percentage of the total analysis time
Free problem	8.70	58%
Interface and link problem	1.95	13%
Post-processing	1.50	10%
Fracture test and topology updating	2.85	19%

5.1.2. Large imposed crack opening displacement

Fig. 23 shows the crack tip position histories, obtained for an initial crack opening displacement $W_0 = 1.2$ μm. At difference with the previous case, no arrest occurs in the propagation of the crack, and both subdomains Ω_1 and Ω_2 are interested by the crack propagation. Consequently, the interface operator has to be re-computed to take into account the change in the integration scheme of subdomains Ω_1 and Ω_2 and the presence of a crossing crack, which causes a change in the interface connectivity. Considering the case of the coarse mesh, the condition number of matrix $\mathbf{H}$ reaches a maximum of 129.49, when the crack has completely crossed the interface between subdomains.

The final deformed shape is depicted in Fig. 24; as in the previous case, the displacements have been magnified by a factor equal to 10.

Fig. 25 shows the energy balance: notice that the introduction of a domain decomposition approach causes a minimal dissipation, on the order of 1.5% of the global energy balance.

Table 4 gives the analysis times and the computational gain. The proposed numerical procedure allows for a reduction respectively of the 34% of the total analysis time with respect to a monolithic finite element simulation.

5.2. Kalthoff's test

As a second example, the numerical simulation of the dynamic crack propagation experiments performed by [53] is carried out. In these tests, mixed-mode dynamic loading conditions were created by means of the technique of loading cracks by edge impact (LECEI), developed by the authors: a specimen with two parallel edge notches is impacted by a projectile moving at a given speed V_0 in the direction parallel to the notch; the diameter of the projectile is equal to the distance between the two notches. This configuration determines a compressive wave that propagates in the middle

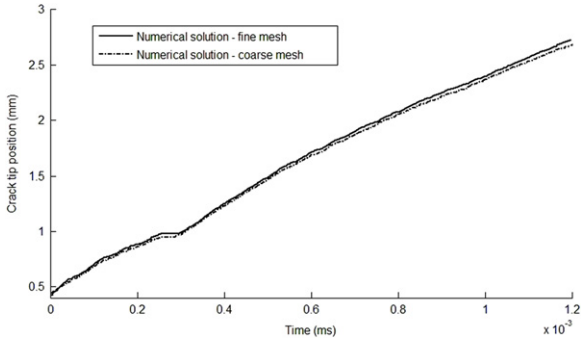

Fig. 23. Double cantilever beam test. Crack tip position: $W_0 = 1.2$ μm.

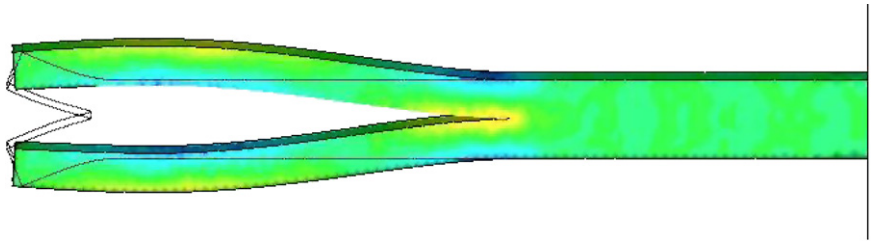

Fig. 24. Double cantilever beam test. Deformed shape: $W_0 = 1.2$ μm.

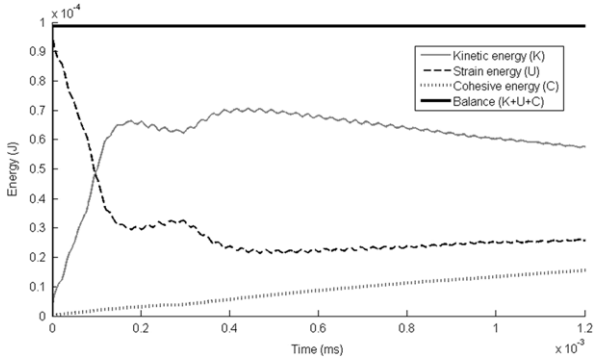

Fig. 25. Double cantilever beam test. Energy balance.

Table 4
Double cantilever beam—large imposed crack opening displacement: analysis times and computational gain (calculations were carried out on an Intel Core i7-870 Cpu@2.93 GHz).

Algorithm	Analysis time (h)	Computational gain
Monolithic analysis	25	–
Domain decomposition	16.5	34%

of the specimen, causing a pure mode II loading condition at the crack tip. The specimen, schematically represented in Fig. 26, is a maraging steel plate 18Ni1900, whose material properties are listed in Table 5. A transition in the failure mode was observed depending on the impact velocity: at low impact velocities, namely below 30 m/s, brittle fracture occurs with a crack propagation angle of about 70°; on the contrary, if the impact velocity increases, the crack propagation is governed by the formation of shear bands ahead of the notch at a negative angle of about 10°. The former case is here considered.

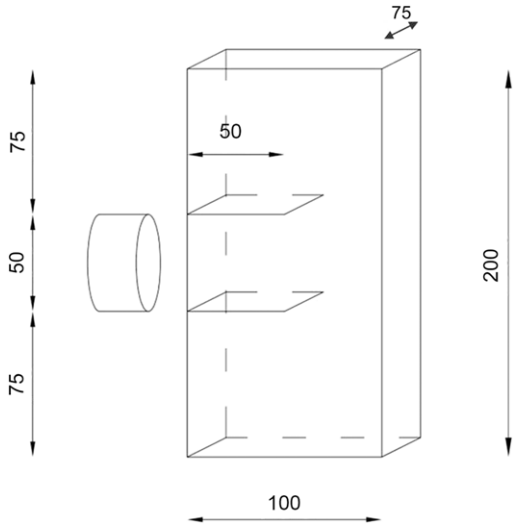

Fig. 26. Kalthoff's experiment. Specimen geometry.

Table 5
Kalthoff's experiment. Material properties of maraging 18Ni1900 steel.

Young's modulus	E	190 GPa
Poisson's coefficient	ν	0.30
Density	ρ	8000 kg/m^3
Fracture energy	G_{I_c}	22,170 N/m
Tensile strength	$t_{\max}$	844 MPa

Table 6
Kalthoff's experiment. Partition into subdomains: number of nodes and elements per subdomain.

Subdomain	Number of elements	Number of nodes
Ω_1	16,535	26,368
Ω_2	16,213	25,419
Ω_3	17,218	26,903
Ω_4	16,671	26,079

The numerical simulation of Kalthoff's experiment has been afforded in several works in the finite element literature. Belytschko et al. [55] faced the problem of brittle failure applying the extended finite element technique (XFEM) on a 2-D finite element model, both with loss of hyperbolicity criterion and tensile stress criterion: the authors reported a crack propagation angle almost equal to 58° in the former case and to 65° in the latter one. These results have been compared by the authors with those deriving from simulations performed with the inter-element technique, modelled with Xu–Needleman's cohesive law [56], in which the fracture propagated with an average angle of almost 55°. The XFEM method was adopted also in [54], in [57], and in [58], obtaining a crack propagation angle of 65°.

Because of the twofold symmetry, only one half of the specimen has been modelled, and in Fig. 27 the adopted finite element mesh is displayed. An average element size of 1 mm, lower than the cohesive process zone length equal to 5.96 mm, has been considered. Symmetric boundary conditions have been imposed at the lower surface of the domain.

The geometrical partition into four subdomains, shown in Fig. 28, has been adopted. Table 6 gives the number of nodes and elements per subdomain. The grid partition determines the presence of 2345 interface nodes.

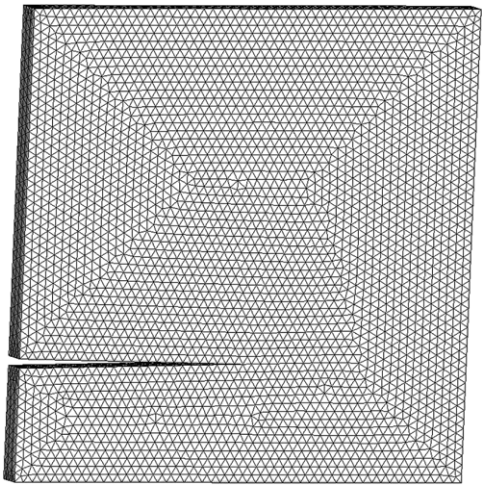

Fig. 27. Kalthoff's experiment. Finite element mesh.

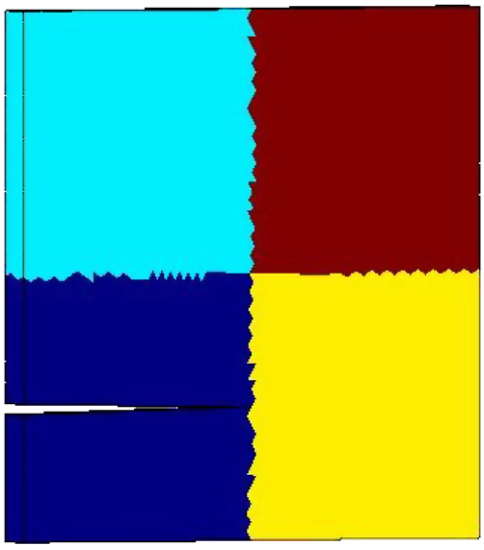

Fig. 28. Kalthoff's experiment. Partition into subdomains.

As shown in Fig. 29, the crack propagates with an average angle of 61°, well in agreement with the experimental data and with the results of the simulation proposed in the literature.

Figs. 30–33 display the time evolution of the crack pattern: in all these figures the deformed shape at the set times is shown on the left, while the contour plot of σ_x component of the stress vector on the right. A deviation in the crack direction can be observed in Fig. 33, because the finite element mesh does not allow for a straight line propagation. The fracture crosses two of the four subdomains: the procedures related to the crack propagation inside a subdomain and across the connectivity interface have therefore been activated in the simulation.

Fig. 34 shows the evolution of the internal energies and of the external work during the test. It is worth emphasizing again, that the dissipation due to the work of the interface forces does not sensibly affect the overall balance; thereby, the dissipation at the connectivity interface between subdomains is small enough compared to the cohesive energy amount (it does not overcome the 2% of the cohesive energy, as shown in Fig. 35).

Table 7 shows the analysis times and the computational gain. The proposed algorithm allows for a reduction of the 38% of the total analysis time with respect to a monolithic simulation.

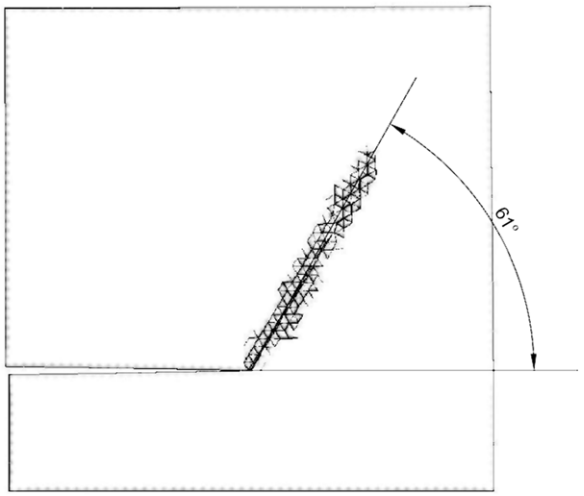

Fig. 29. Kalthoff's experiment. Crack propagation angle.

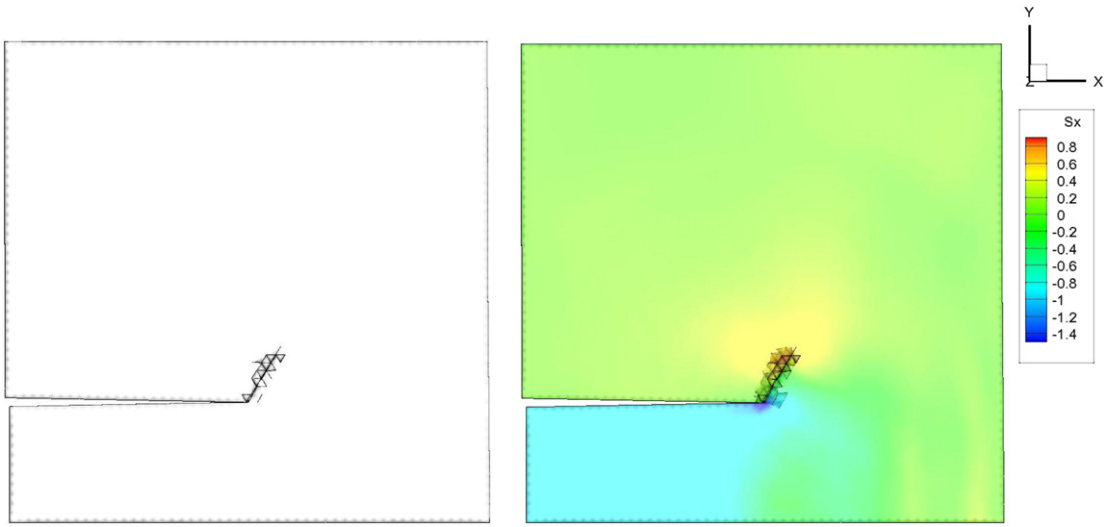

(a) Deformed shape. (b) Stress σ_x.

Fig. 30. Kalthoff's experiment. $t = 0.3$ μs.

Table 7
Kalthoff's experiment: analysis times and computational gain (calculations were carried out on an Intel Core i7-870 Cpu@2.93 GHz).

Algorithm	Analysis time (h)	Computational gain
Monolithic analysis	46	–
Domain decomposition	28.5	38%

5.3. Polycrystalline single edge notched specimen

In this section we consider a polysilicon notched specimen, see Fig. 36, elongated at both ends by a linear increasing displacement of 32 nm in 10^{-3} μs. The specimen is 8 μm long and 0.4 μm thick, while its width varies from a maximum of 1 μm to a minimum of 0.6 μm reached at the notch level. The analysis domain has been discretized with 138,062 tetrahedral elements and 196,253 nodes (see Fig. 37). As introduced in Section 2, the elastic bulk behaviour

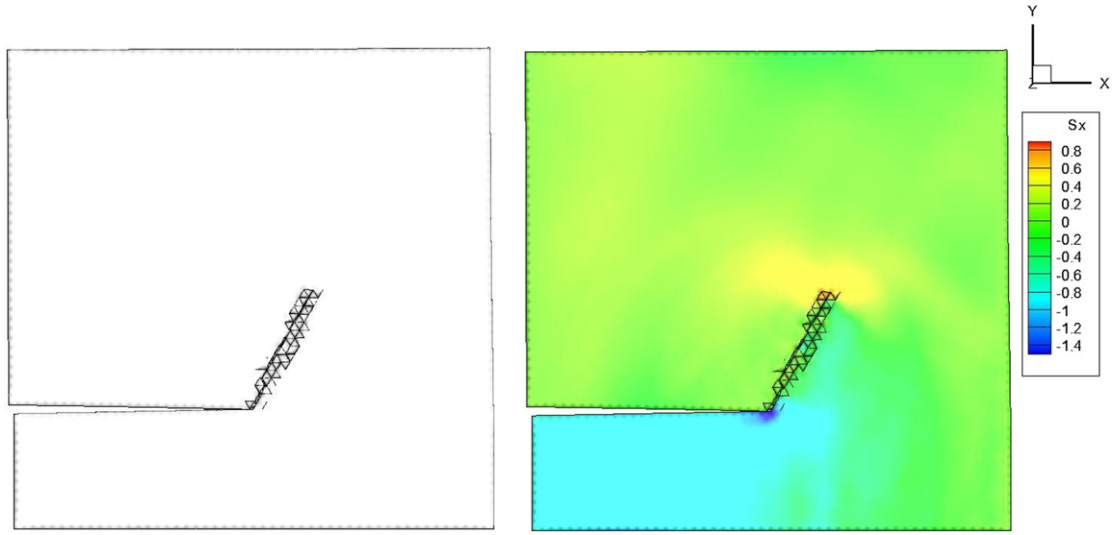

(a) Deformed shape. (b) Stress σ_x.

Fig. 31. Kalthoff's experiment. $t = 0.4$ µs.

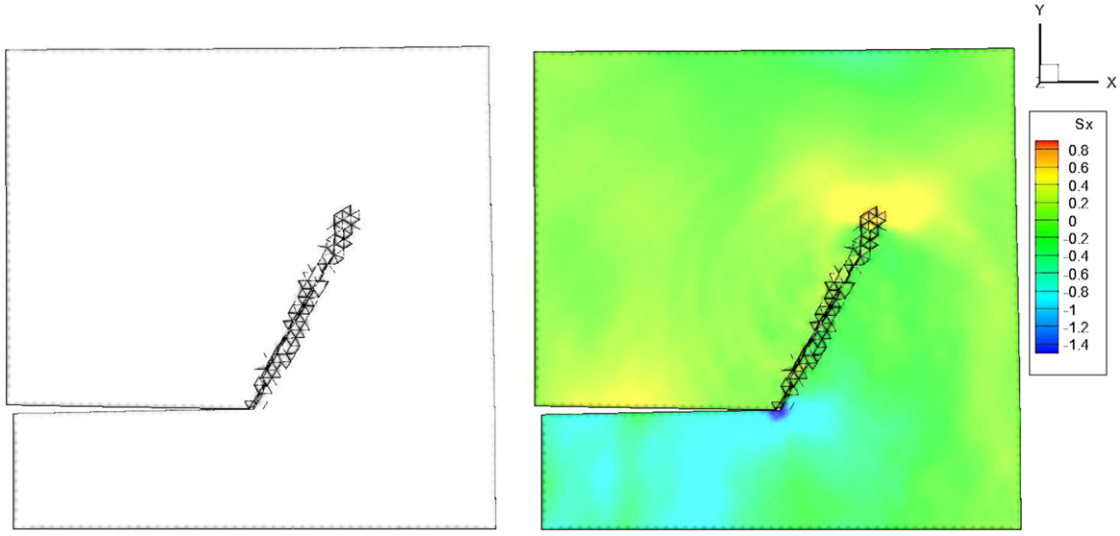

(a) Deformed shape. (b) Stress σ_x.

Fig. 32. Kalthoff's experiment. $t = 0.5$ µs.

of each grain is described by a linear elastic transversely isotropic law, characterized by the elastic constants proposed in [59]: $s_{11} = 165.7$ GPa, $s_{12} = 63.9$ GPa, and $s_{44} = 79.6$ GPa (see Eq. (9)). The assumed cohesive interface law is characterized by a fracture energy $G_c = 7.0 \cdot 10^{-3}$ N/mm and a maximum tensile stress $t_{\max} = 2.5$ GPa, both for the grain and for the grain boundaries. The implicit time step has been taken equal to 1000 times the explicit one $\Delta t_{expl} = 2 \cdot 10^{-14}$ s.

Two partition methods, the first based on the collection of silicon grains, and the second one derived by the automatic partition algorithm, have been explored. Fig. 38 shows the resulting mesh decompositions, each colour representing a single subdomain, and Tables 8 and 9 show the number of elements and of degrees of freedom per subdomain, obtained, respectively, with an automatic and with a grain-based partition of the body into four

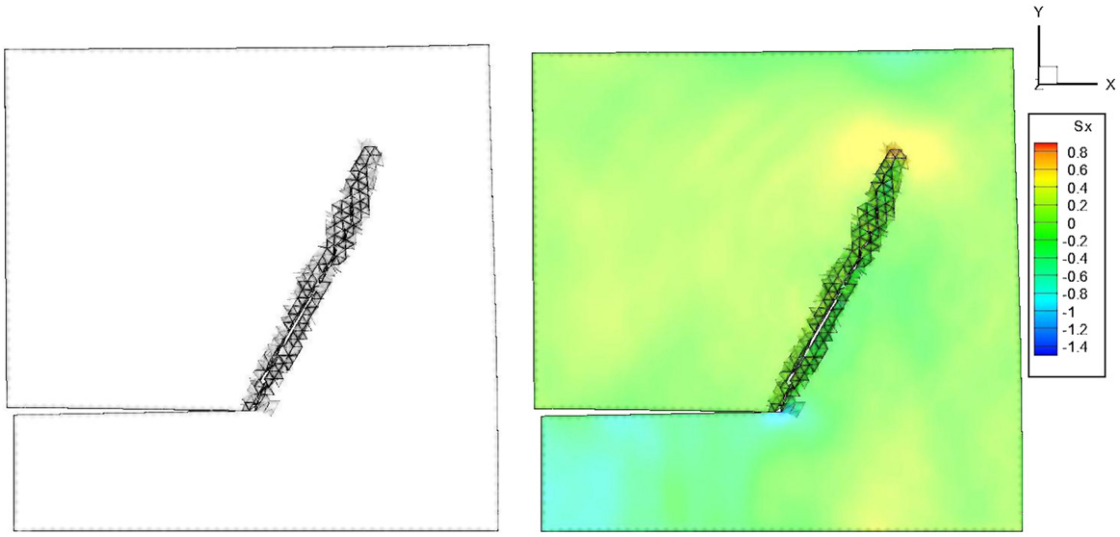

(a) Deformed shape. (b) Stress σ_x.

Fig. 33. $t = 0.6\,\mu s$.

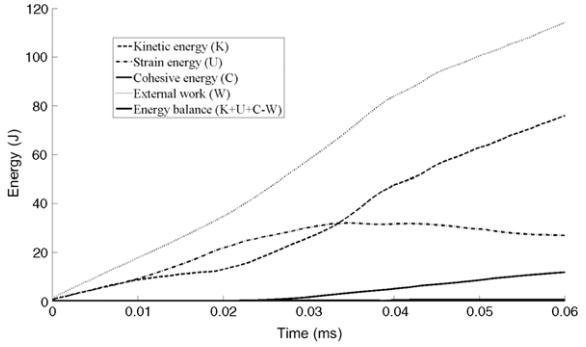

Fig. 34. Kalthoff's experiment. Energy balance.

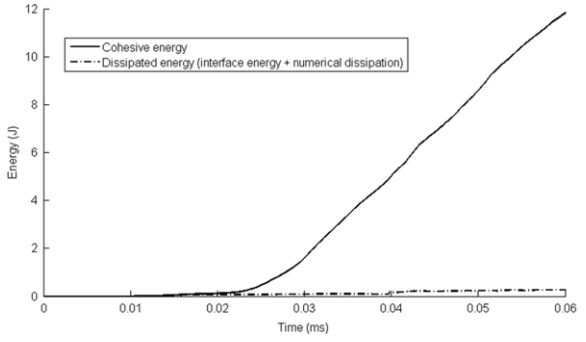

Fig. 35. Kalthoff's experiment. Comparison between the amount of cohesive and dissipated energies.

subdomains. Notice that in the second case there is a great difference in the number of elements per subdomain, due to the non uniform discretization of the domain.

Figs. 39–41 show the crack pattern at five subsequent time instants. For each time instant, a top view of the deformed shape (on the left), the contour plot of the stress in the load direction (on the right), and a front view detail of the notch (on the bottom) are displayed. The crack starts at the upper surface in correspondence of the re-

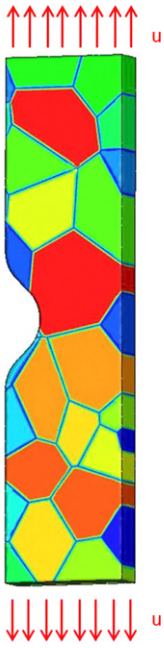

Fig. 36. Single edge notched specimen subjected to uniform displacement at both the edges.

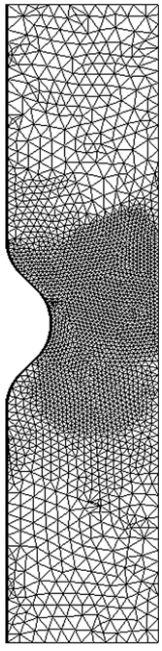

Fig. 37. Single edge notched specimen. Finite element discretization.

entrant lateral surface, then it becomes through-thickness while, at the same time, it propagates inside the bulk. A rather diffused cracking is also observed in the neighbouring of the dominant fracture; the longitudinal stress tends to remain rather low except for a very small region (not visible in the figures) near the crack tip, as expected for quasi-brittle fracture.

Fig. 42 displays the comparison between the crack patterns obtained with the proposed domain decomposition algorithm, respectively with automatic partitioning (a) and grain-based partitioning (b), and the result of a monolithic

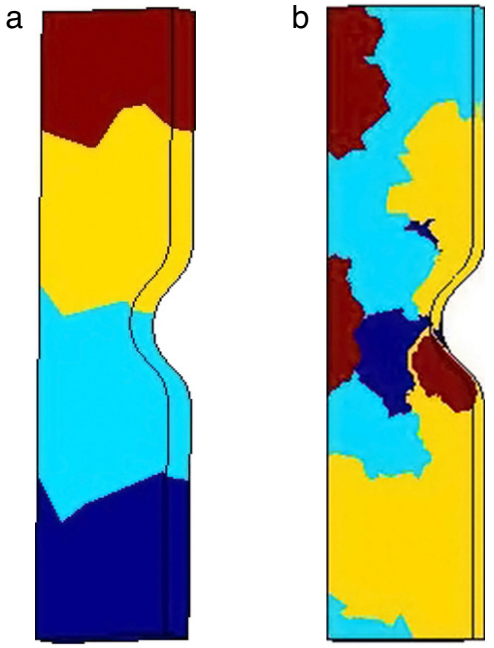

Fig. 38. Single edge notched specimen. Adopted mesh subdivision: (a) grain-based and (b) automatic partition. (For interpretation of the references to colour in this figure legend, the reader is referred to the web version of this article.)

Table 8
Single edge notched specimen: automatic partition details.

Subdomain	Number of elements	Number of nodes
Ω_1	34,516	51,659
Ω_2	34,516	53,379
Ω_3	34,516	53,708
Ω_4	34,514	52,041

Table 9
Single edge notched specimen: grain-based partition details.

Subdomain	Number of elements	Number of nodes
Ω_1	11,508	19,784
Ω_2	70,429	70,429
Ω_3	63,793	97,099
Ω_4	10,200	16,477

finite element simulation (c). A good agreement can be observed; the small discrepancies are due to the small corrections between subdomains created by the solution of the interface problem.

A quantitative comparison between the domain decomposition solution (obtained with a grain-based partition) and the monolithic one can be found in Fig. 43, where the reaction force computed at the upper surface as a function of the imposed displacement is depicted. Again, the major discrepancy arises only near the end of the analysis, when the effects of the corrections at the interfaces are emphasized.

As it can be seen from Fig. 44, where the energy balance is reported, the numerical dissipation due to the work of interface forces does not exceed the 2% of the total energy in the system, and it can be considered sufficiently small if compared with the cohesive energy.

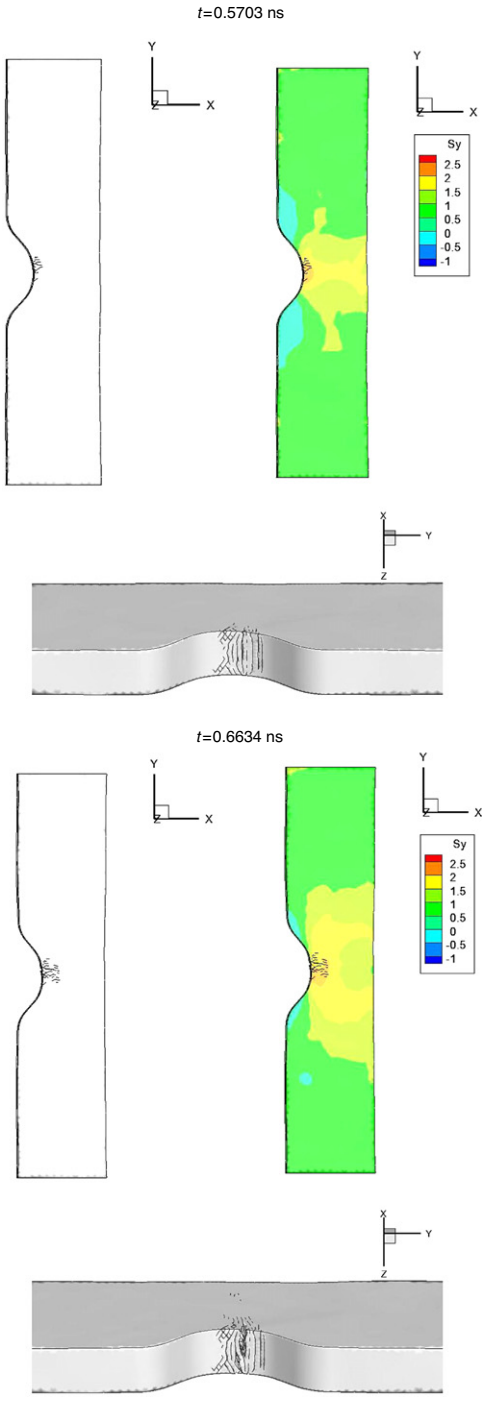

Fig. 39. Single edge notched specimen: evolution of the fracture process.

Table 10 gives the analysis times and the computational gain obtained with the two partition techniques. It is worthwhile to underline that the proposed numerical procedure allows for a reduction respectively of the 42% and of the 38% of the total analysis time with respect to a standard finite element simulation, even with a poor parallelization, here not described. It can be also observed that, in the case of the automatic partition, the crack propagation involves three subdomains, while in the case of the grain-based partition only two subdomains are crossed by the fracture.

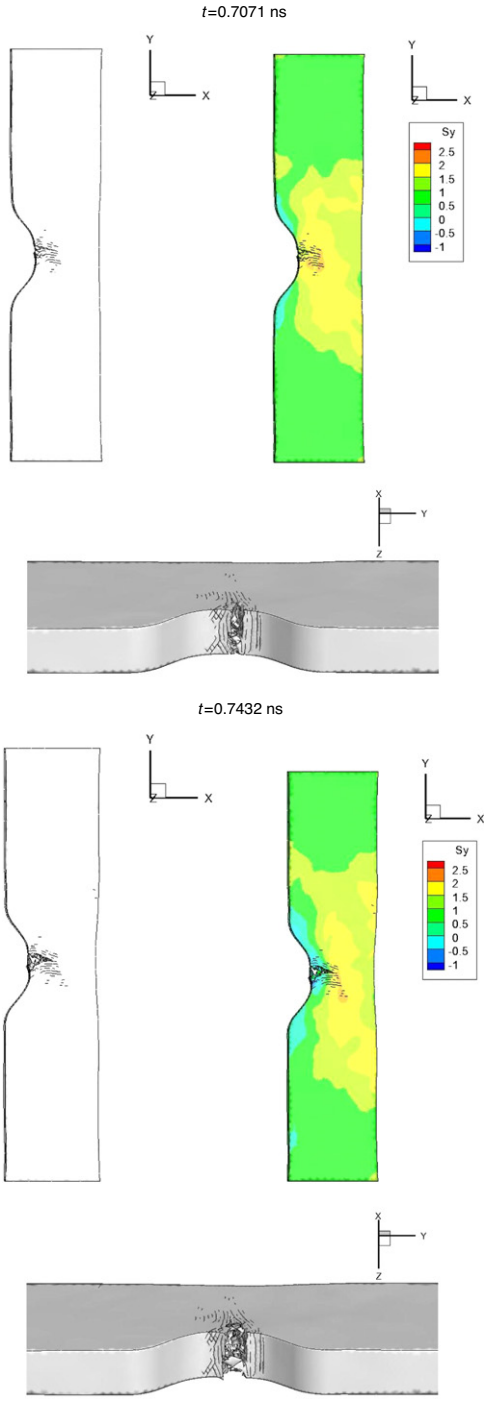

Fig. 40. Single edge notched specimen: evolution of the fracture process.

5.4. Dogbone specimen

The dogbone specimen, shown in Fig. 45, constrained at the bottom and elongated at the upper surface, is considered. The sample is 10 μm high and 1 μm thick; its width varies from a maximum of 2 μm at the bottom and at the upper surface, to a minimum of 2 μm in the middle of the specimen. The analysis domain has been discretized with

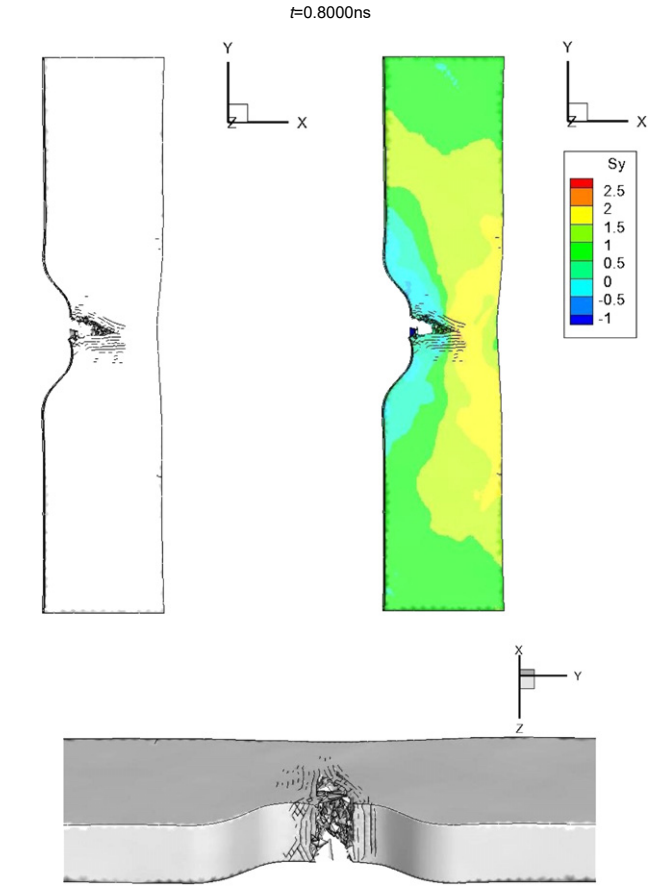

Fig. 41. Single edge notched specimen: final crack pattern.

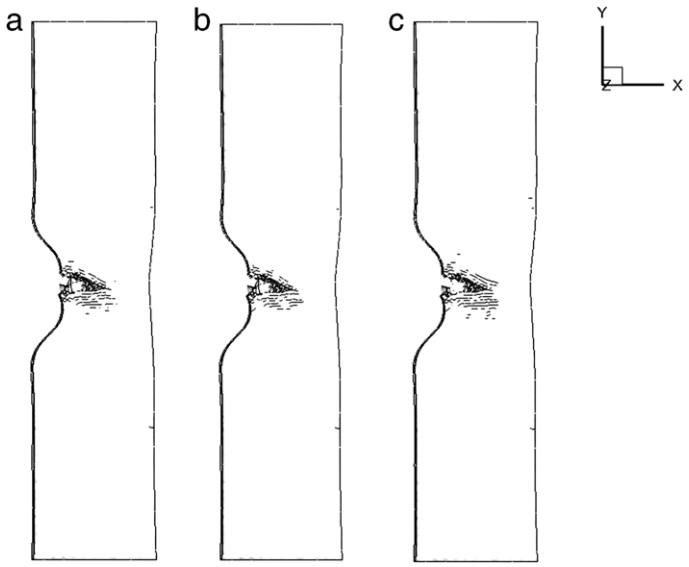

Fig. 42. Single edge notched specimen; crack pattern comparison: (a) grain-based partitioning, (b) automatic partitioning, (c) monolithic solution.

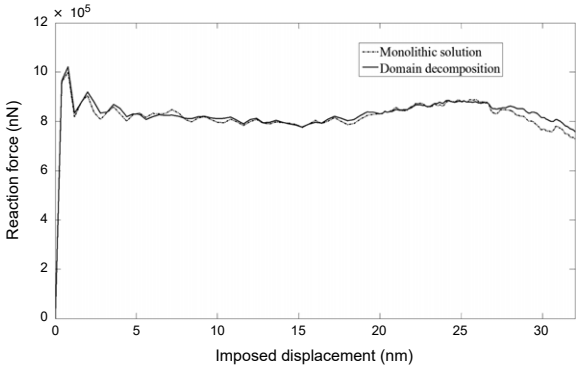

Fig. 43. Single edge notch specimen: evolution of the reaction force with the imposed displacement.

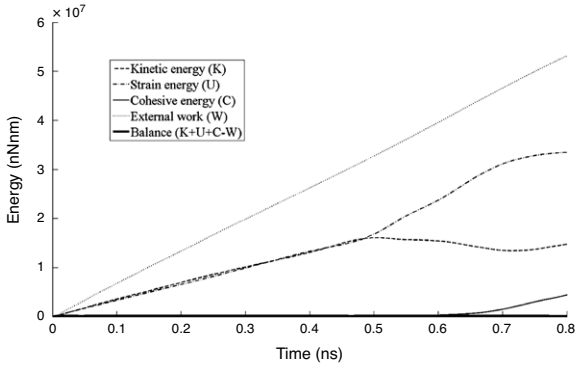

Fig. 44. Single edge notch specimen: energy balance.

Table 10
Single edge notch specimen: analysis times and computational gain (calculations were carried out on an Intel Core i7-870 Cpu@2.93 GHz).

Algorithm	Partitioning technique	Analysis time (h)	Computational gain
Monolithic analysis		120	–
Domain decomposition	Automatic partition	74	38%
Domain decomposition	Partition by grains	70	42%

44,265 tetrahedral elements, as shown in Fig. 46. The specimen is elongated by an imposed displacement, linearly increasing from 0 to 135 nm. The analysis time is equal to 0.45 μs.

The example proposed in this section shows the capability of the implemented code to reproduce an intergranular crack propagation, while the crack path of the previous case was mainly transgranular: works carried out by Ballarini et al. [60] and Chasiotis and Knauss [61] have indeed demonstrated that polysilicon films can display both failure mechanisms. This is obtained by introducing a defective grain surface, characterized by lower maximum tensile stress than the grains: $t_{\max} = 1.5$ GPa has been indeed assigned to the grain boundaries, while for the grains it has been taken equal to 2 GPa. The same value of energy fracture, $G_c = 7.0 \cdot 10^{-3}$ N/mm, has been considered both for the grains and for the grain boundary. Regarding the bulk behaviour of polysilicon, the value of the elastic constants proposed in [59] have been considered: $s_{11} = 165.7$ GPa, $s_{12} = 63.9$ GPa, and $s_{44} = 79.6$ GPa. Furthermore, the mass density $\rho = 2330 \ \frac{\text{kg}}{\text{m}}^3$ of polysilicon is assigned.

Fig. 47 shows the crack pattern at four subsequent time instants. As expected, crack propagation occurs along the grain boundaries.

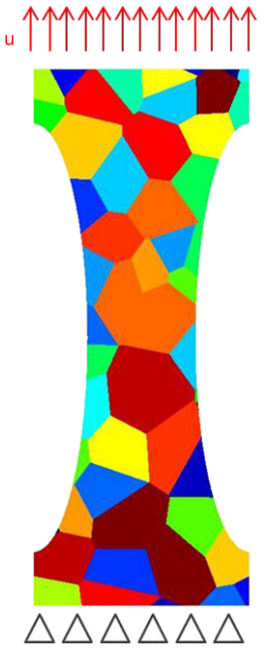

Fig. 45. Dogbone specimen geometry and boundary conditions.

Fig. 46. Dogbone specimen: finite element mesh.

The simulation has been performed with two different mesh partitioning techniques, namely a grain-based partition and an element-size based partition. The obtained subdomains and the details of the partitions are represented in Fig. 48 and listed in Tables 11 and 12.

Table 13 gives the analysis times for the simulations performed with two three partitioning techniques and the computational gain with respect to the monolithic finite element computation. It can be noted that the computational gain reaches the 40% and it is obtained with a grain partition into 4 subdomains: non linearity indeed affects only two

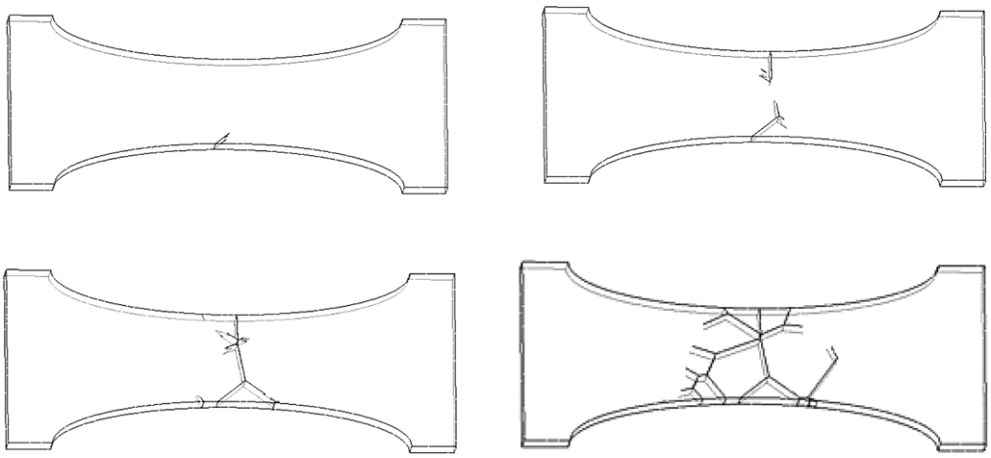

Fig. 47. Evolution of the cracking process.

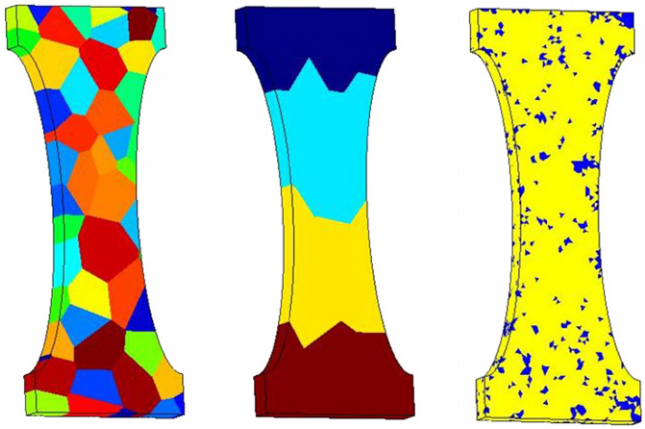

Fig. 48. Dogbone specimen; grain morphology, partition by grains and element size based partitioning.

Table 11
Dogbone specimen; partitioning by grains: number of nodes and elements per subdomain.

Subdomain	Number of elements	Degrees of freedom
Ω_1	10,665	48,582
Ω_2	11,675	54,906
Ω_3	10,175	48,421
Ω_4	11,750	53,142

Table 12
Dogbone specimen; partitioning by element size: number of nodes and elements per subdomain.

Subdomain	Number of elements	Degrees of freedom
Ω_1	39,760	195,087
Ω_2	4,505	64,623

of the four subdomains, created with this partitioning technique. Regarding the element-size based partition technique, it can be observed that the crack propagation reaches both the “big” and the “small” elements, so the reference time

Table 13
Dogbone specimen—weak grain boundaries case: analysis times (Intel Corei7-870 Cpu @ 2.93 GHz).

Algorithm	Partitioning technique	Analysis time (h)	Computational gain
Monolithic analysis		96	–
Domain decomposition	Partition by grains	57	−40%
Domain decomposition	Partition by element size	71	−26%

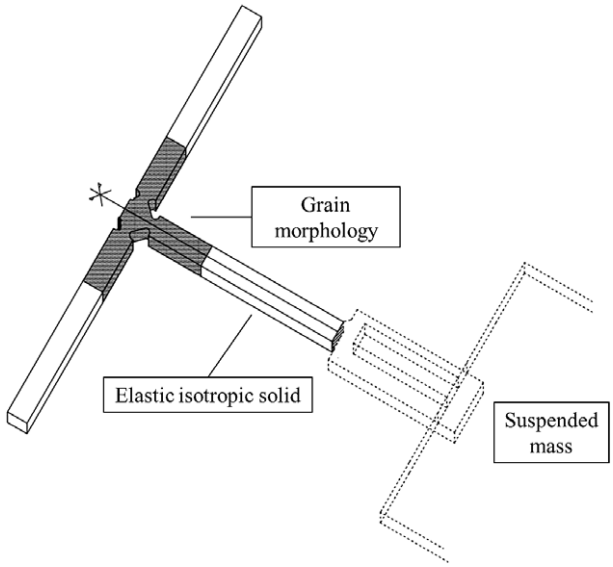

Fig. 49. MEMS detail subject to bending. Suspended mass hitting a polysilicon beam element at the meso-scale level.

scale coincides with the fine explicit time scale, with a time step governed by the CFL condition related to the small element size; this justifies the lower performance of the this partitioning method.

5.5. A MEMS structural detail subject to bending loading conditions

This example addresses the simulation of fracture propagation in a notched region of a polysilicon beam element, subject to a bending loading condition, caused by a tilting suspension mass, hitting its free enlarged end, as shown in Fig. 49. The analysis focuses only on the detail, represented in Fig. 49 with continuous lines. The action of the mass of the structure is taken into account imposing an history of displacement on the dashed surface. As in the previous example, the input displacement, has been recorded during an elastic analysis performed at the meso-scale on the whole microsystem, imposing a drop acceleration to the mass.

Fig. 50 represents the structure geometry and the boundary conditions. Only the grey zone, nearby the two notches, loci of possible fracture nucleation, have been considered as polycrystalline, while elastic isotropic bodies have been considered far from them. The grain morphology is shown in Fig. 51.

As in previous example, the polysilicon bulk behaviour has been described by an anisotropic constitutive behaviour characterized by the three elastic constants, $s_{11} = 165.7$ GPa, $s_{12} = 63.9$ GPa, and $s_{44} = 79.6$ GPa; the mass density ρ has been considered equal to 2330 $\frac{\text{kg}}{\text{m}}^3$; the same parameters have been adopted for the cohesive behaviour both in case of trans- and inter-granular fractures. The cohesive length can thus be estimated with reference to a homogeneous value of Young's modulus of polysilicon, assumed equal to 150 GPa, obtaining $l_c = 168$ μm. The structural element has been meshed with an average element size equal to 100 nm, decreased up to 40 nm in the critical zone near the two notches. The cohesive length is thus fully resolved. The overall finite element mesh, characterized by 177,177 elements and 254,447 nodes, is represented in Fig. 52.

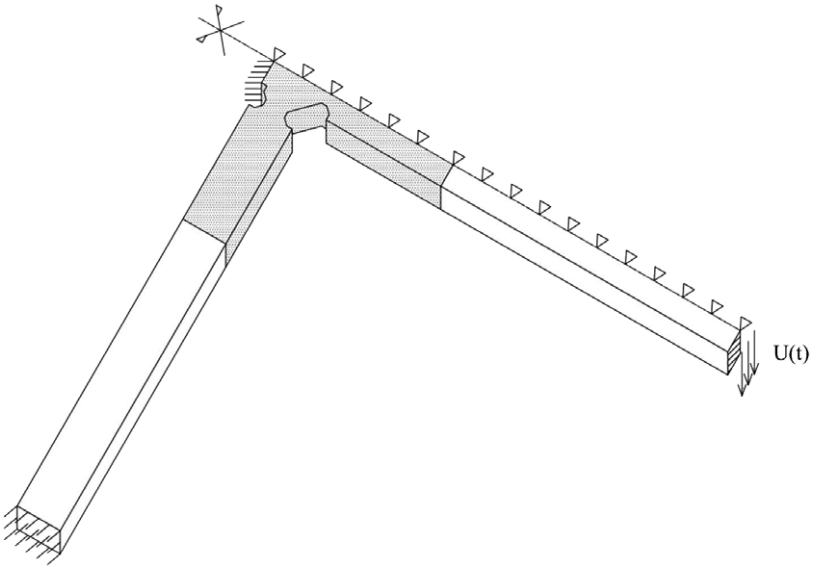

Fig. 50. MEMS structural detail: geometry.

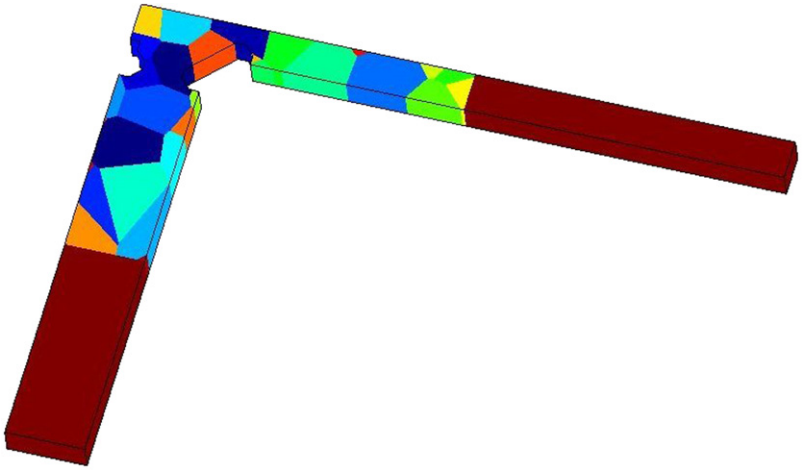

Fig. 51. MEMS detail subject to bending: grain morphology.

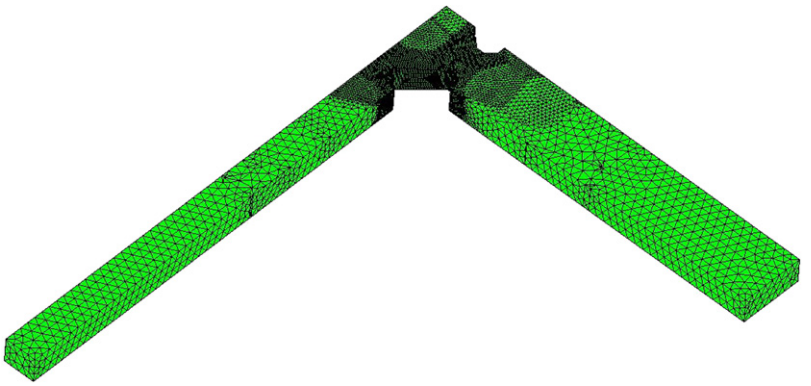

Fig. 52. MEMS structural detail: finite element mesh.

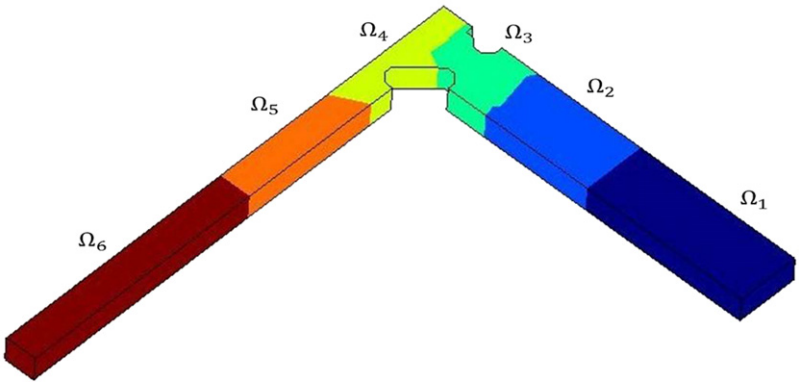

Fig. 53. Partition into subdomains.

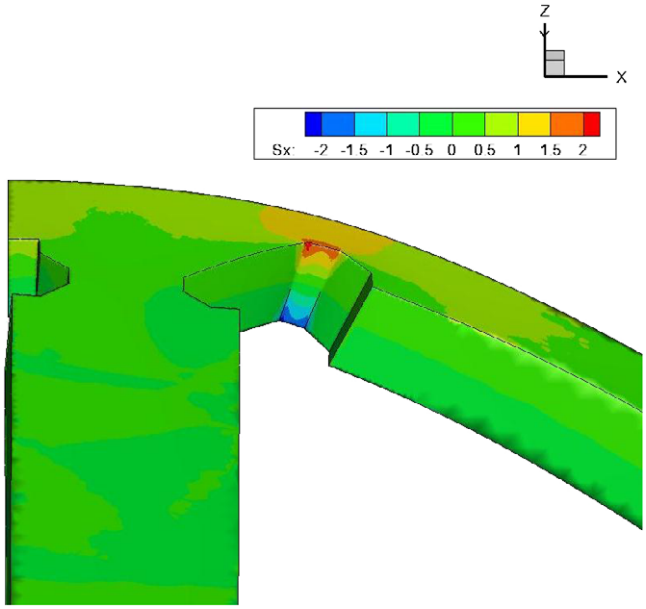

Fig. 54. Contour plot of the normal stress component in direction x at the onset of the crack.

Table 14
Degrees of freedom for each subdomain for grain-based partition.

Subdomain	Number of elements	Number of nodes	Degrees of freedom
1	2,131	3,863	11,066
2	2,610	4,541	13,292
3	75,471	109,198	323,351
4	85,349	121,868	364,506
5	8,597	13,343	40,021
6	3,019	5,119	14,952

The domain has been partitioned into six subdomains, sketched in Fig. 53. A grain-based partition has been employed, since the presence of the notches suggests which region will be loci of crack initiation. The details of the partition in terms of number of elements, nodes and degrees of freedom are reported in Table 14. Notice that the subdomains Ω_3 and Ω_4 contain a sensibly higher number of elements than the others; this is due to the non uniform adopted discretization.

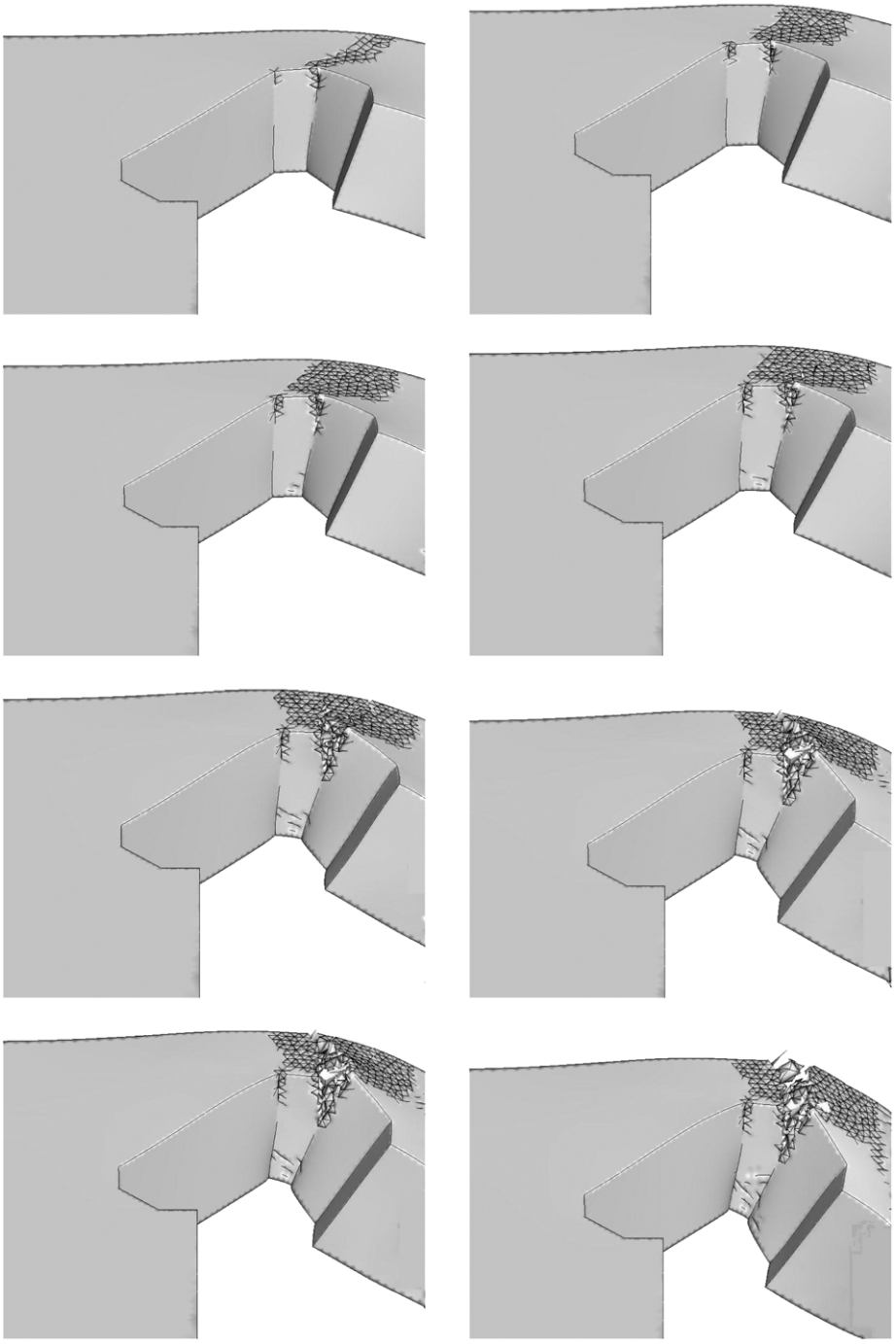

Fig. 55. Evolution of the cracking process.

The presence of the two notches create a concentration in the stress, that leads to fracture initiations. Fig. 54 shows the contour plot of the normal stress component in the direction x at the onset of the crack.

Fig. 55 shows the crack patterns at eight subsequent time instants. As expected, crack develops in correspondence of one of the two notches in the tensed upper part of the beam and develops inside subdomain Ω_4. The depicted deformed shapes have been obtained by amplifying the displacements by a factor equal to 10.

6. Conclusions

A domain decomposition technique in structural dynamics has been here extended to simulation of fracture processes in polycrystalline continua in the framework of a discrete crack, cohesive approach. The method has been developed with the primary objective of reducing the computational burden in the analysis of polycrystalline solids for microsystems, mainly for polycrystalline silicon, but it can be also applied to other brittle or quasi-brittle materials with little effort. On the contrary, no elasto-plastic model is implemented, so the procedure here presented cannot be directly applied to polycrystalline materials displaying crystal plasticity, like metallic alloys.

The characteristics of the method are: non-overlapping partition in sub-domains, implicit to explicit time integration switching whenever a fracture arises in an intact domain, multi time-step algorithm for the simultaneous solution of implicit and explicit problems. At the present time only two time steps have been considered: one for the implicit subdomains and the other for the explicit ones. It could be useful to introduce a different explicit time step for each subdomain, evaluated on the basis on the CFL condition. On the other hand, an explicit time step variable in time, as proposed in the literature, for instance, by [62–65], would be difficult to handle in this framework. The paper discusses the alternative formulations in cases of fracture(s) propagating inside or across or in-between the sub-domains, and it provides numerical examples for the validation of the method and its application to microsystem problems.

Work in progress includes an efficient exploitation of parallel computing strategies, application of domain decomposition techniques to multi-physics problems and combination of domain decomposition techniques with Model Order Reduction ones.

Acknowledgement

Part of this work has been carried out in the framework of Eniac Joint Undertaking Project: Lab4MEMS, grant no. 325622.

References

[1] A. Corigliano, F. Cacchione, A. Frangi, S. Zerbini, Numerical modelling of impact rupture in polysilicon microsystems, Comput. Mech. 42 (2007) 251–259.

[2] S. Mariani, A. Ghisi, A. Corigliano, S. Zerbini, Multi-scale analysis of MEMS sensors subject to drop impacts, Sensors 7 (2007) 1817–1833.

[3] A. Gravouil, A. Combescure, Multi-time-step explicit–implicit method for non-linear structural dynamics, Int. J. Numer. Methods Eng. 50 (2001) 199–225.

[4] N. Mahjoubi, A. Gravouil, A. Combescure, N. Greffet, A monolithic energy conserving method to couple heterogeneous time integrators with incompatible time steps in structural dynamics, Comput. Methods Appl. Mech. Engrg. 200 (2011) 1069–1086.

[5] C. Farhat, F. Roux, A method for finite element tearing and interconnecting and its parallel solution algorithm, Int. J. Numer. Methods Eng. 32 (1991) 1205–1227.

[6] O. Lloberas-Valls, D. Rixen, A. Simone, L. Sluys, Domain decomposition techniques for the efficient modeling of brittle heterogeneous materials, Comput. Methods Appl. Mech. Engrg. 200 (2011) 1577–1590.

[7] J. Pebrel, C. Rey, P. Gosselet, A nonlinear dual-domain decomposition method: application to structural problems with damage, Int. J. Multiscale Comput. Eng. 6 (2008) 251–262.

[8] P. Kerfriden, O. Allix, P. Gosselet, A three-scale domain decomposition method for the 3D analysis of debonding in laminates, Comput. Mech. 44 (2009) 343–362.

[9] Y. Fragakis, M. Papadrakakis, The mosaic of high performance domain decomposition methods for structural mechanics: formulation, interrelation and numerical efficiency of primal and dual methods, Comput. Methods Appl. Mech. Engrg. 192 (2003) 3799–3830.

[10] P. Gosselet, C. Rey, Non-overlapping domain decomposition methods in structural mechanics, Arch. Comput. Methods Eng. 13 (2006) 515–572.

[11] F. Confalonieri, G. Cocchetti, A. Ghisi, A. Corigliano, A domain decomposition method for the simulation of fracture in polysilicon MEMS, Microelectron. Reliab. 58 (2013) 1045–1054.

[12] P.D. Zavattieri, H.D. Espinosa, Grain level analysis of crack initiation and propagation in brittle materials, Acta Mater. (2001).

[13] H.D. Espinosa, P.D. Zavattieri, A grain level model for the study of failure initiation and evolution in polycrystalline brittle materials. Part II: Numerical examples, Mech. Mater. 35 (2003) 365–394.

[14] S. Ghosh, Z. Nowak, K. Lee, Tessellation-based computational methods for the characterization and analysis of heterogeneous microstructures, Compos. Sci.Technol. 57 (1997) 1187–1210.

[15] J.R. Li, J.L. Yu, Computational simulations of intergranular fracture of polycrystalline materials and size effect, Eng. Fract. Mech. 72 (2005) 2009–2017.

[16] N. Sukumar, D.J. Srolovitz, T.J. Baker, J.H. Prevost, Brittle fracture in polycrystalline microstructures with the extended finite element method, Int. J. Numer. Methods Eng. 56 (2003) 2015–2037.

[17] M. Paggi, P. Wriggers, A nonlocal cohesive zone model for finite thickness interfaces—Part I: Mathematical formulation and validation with molecular dynamics, Comput. Mater. Sci. 50 (2011) 1625–1633.

[18] Z. Shabir, E. Van der Giessen, C.a. Duarte, a. Simone, The role of cohesive properties on intergranular crack propagation in brittle polycrystals, Model. Simul. Mater. Sci. Eng. 19 (2011) 035006.
[19] R. Mullen, R. Ballarini, Y. Yin, A. Heuer, Monte Carlo simulation of effective elastic constants of polycrystalline thin films, Acta Mater. 45 (1997) 2247–2255.
[20] S. Mahadevan, Y. Zhao, Advanced computer simulation of polycrystalline microstructure, Comput. Methods Appl. Mech. Engrg. 191 (2002) 3651–3667.
[21] S. Weyer, A. Frohlich, H. Riesch-Oppermann, L. Cizelj, M. Kovac, Automatic finite element meshing of planar Voronoi tessellations, Eng. Fract. Mech. 69 (2002) 945–958.
[22] H.D. Espinosa, P.D. Zavattieri, A grain level model for the study of failure initiation and evolution in polycrystalline brittle materials. Part I: Theory and numerical implementation, Mech. Mater. 35 (2003) 333–364.
[23] S. Li, S. Ghosh, Extended Voronoi cell finite element model for multiple cohesive crack propagation in brittle materials, Int. J. Numer. Methods Eng. 65 (2006) 1028–1067.
[24] T. Luther, C. Könke, Polycrystal models for the analysis of intergranular crack growth in metallic materials, Eng. Fract. Mech. 76 (2009) 2332–2343.
[25] R. Quey, P. Dawson, F. Barbe, Large-scale 3D random polycrystals for the finite element method: generation, meshing and remeshing, Comput. Methods Appl. Mech. Engrg. 200 (2011) 1729–1745.
[26] S. Mariani, A. Ghisi, A. Corigliano, R. Martini, B. Simoni, Two-scale simulation of drop-induced failure of polysilicon MEMS sensors, Sensors 11 (2011) 4972–4989.
[27] G.T. Camacho, M. Ortiz, Computational modelling of impact damage in brittle materials, Int. J. Solids Struct. 33 (1996) 2899–2938.
[28] M. Ortiz, A. Pandolfi, Finite-deformation irreversible cohesive elements for three-dimensional crack propagation analysis, Int. J. Numer. Methods Eng. 44 (1999) 1267–1282.
[29] R.H. Kraft, J.F. Molinari, A statistical investigation of the effects of grain boundary properties on transgranular fracture., Acta Mater. 56 (2008) 4739–4749.
[30] F. Zhou, J.F. Molinari, Dynamic crack propagation with cohesive elements: a methodology to address mesh dependency, Int. J. Numer. Methods Eng. 59 (2004) 1–24.
[31] G.K. Sfantos, M.H. Aliabadi, A boundary cohesive grain element formulation for modelling intergranular microfracture in polycrystalline brittle materials, Int. J. Numer. Methods Eng. 69 (2007) 1590–1626.
[32] R. Kraft, J. Molinari, K. Ramesh, D. Warner, Computational micromechanics of dynamic compressive loading of a brittle polycrystalline material using a distribution of grain boundary properties, J. Mech. Phys. Solids 56 (2008) 2618–2641.
[33] M. Tanaka, K. Higashida, H. Nakashima, H. Takagi, M. Fujiwara, Orientation dependence of fracture toughness measured by indentation methods and its relation to surface energy in single crystal silicon, Int. J. Fract. 139 (2006) 383–394.
[34] S. Mariani, A. Ghisi, F. Fachin, F. Cacchione, A. Corigliano, S. Zerbini, A three-scale FE approach to reliability analysis of MEMS sensors subject to impacts, Meccanica 43 (2008) 469–483.
[35] S. Mariani, A. Ghisi, A. Corigliano, S. Zerbini, Modeling impact-induced failure of polysilicon MEMS: a multi-scale approach, Sensors 9 (2009) 556–567.
[36] A. Prakash, K.D. Hjelmstad, A FETI-based multi-time-step coupling method for Newmark schemes in structural dynamics, Int. J. Numer. Methods Eng. 61 (2004) 2183–2204.
[37] B. Herry, L. Di Valentin, A. Combescure, An approach to the connection between subdomains with non-matching meshes for transient mechanical analysis, Int. J. Numer. Methods Eng. 55 (2002) 973–1003.
[38] V. Faucher, A. Combescure, A time and space mortar method for coupling linear modal subdomains and non-linear subdomains in explicit structural dynamics, Comput. Methods Appl. Mech. Engrg. 192 (2003) 509–533.
[39] A. Combescure, A. Gravouil, B. Herry, An algorithm to solve transient structural non-linear problems for non-matching time-space domains, Comput. Struct. 81 (2003) 1211–1222.
[40] C. Farhat, F. Roux, L. Crivelli, A transient FETI methodology for large-scale parallel implicit computations in structural mechanics, Int. J. Numer. Methods Eng. 37 (1994) 1945–1975.
[41] D.J. Rixen, C. Farhat, A simple and efficient extension of a class of substructure based preconditioners to heterogenous structural mechanics problems, Int. J. Numer. Methods Eng. 516 (1999) 489–516.
[42] P. Gosselet, C. Rey, D. Rixen, On the initial estimate of interface forces in feti methods, Comput. Methods Appl. Mech. Engrg. 192 (2003) 2749–2764.
[43] A. Pandolfi, M. Ortiz, Solid modeling aspects of three-dimensional fragmentation, Eng. Comput. 14 (1998) 287–308.
[44] A. Pandolfi, M. Ortiz, An efficient adaptive procedure for three-dimensional fragmentation simulations, Eng. Comput. 18 (2002) 148–159.
[45] W. Celes, G.H. Paulino, R. Espinha, A compact adjacency-based topological data structure for finite element mesh representation, Int. J. Numer. Methods Eng. 64 (2005) 1529–1556.
[46] G.H. Paulino, W. Celes, R. Espinha, Z.J. Zhang, A general topology-based framework for adaptive insertion of cohesive elements in finite element meshes, Eng. Comput. 24 (2007) 59–78.
[47] C. Farhat, A simple and efficient automatic FEM domain decomposer, Comput. Struct. 28 (1988) 579–602.
[48] D. Vanderstraeten, R. Keunings, Optimized partitioning of unstructured finite element meshes, Int. J. Numer. Methods Eng. 38 (1995) 433–450.
[49] F. Casadei, J.P. Halleux, Binary spatial partitioning of the central-difference time integration scheme for explicit fast transient dynamics, Int. J. Numer. Methods Eng. 78 (2009) 1436–1473.
[50] M. Kanninen, A dynamic analysis of unstable crack propagation and arrest in the DCB test specimen, Int. J. Fract. 10 (1974) 415–430.
[51] K. Hellan, Debond dynamics of an elastic strip, I: Timoshenko-beam properties and steady motion, Int. J. Fract. 14 (1978) 91–100.
[52] L. Freund, Dynamic Fracture Mechanics, Cambridge University Press, Cambridge, 1990.
[53] J.F. Kalthoff, Modes of dynamic shear failure in solids, Int. J. Fract. 101 (2000) 1–31.

[54] J. Réthoré, A. Gravouil, A. Combescure, An energy-conserving scheme for dynamic crack growth using the eXtended finite element method, Int. J. Numer. Methods Eng. 63 (2005) 631–659.
[55] T. Belytschko, H. Chen, J. Xu, G. Zi, Dynamic crack propagation based on loss of hyperbolicity and a new discontinuous enrichment, Int. J. Numer. Methods Eng. 58 (2003) 1873–1905.
[56] X.P. Xu, A. Needleman, Numerical simulations of fast crack growth in brittle solids, J. Mech. Phys. Solids 42 (1994) 1397–1434.
[57] T. Menouillard, J. Réthoré, a. Combescure, H. Bung, Efficient explicit time stepping for the eXtended Finite Element Method (X-FEM), Int. J. Numer. Methods Eng. 68 (2006) 911–939.
[58] T. Elguedj, A. Gravouil, H. Maigre, An explicit dynamics extended finite element method. Part 1: Mass lumping for arbitrary enrichment functions, Comput. Methods Appl. Mech. Engrg. 198 (2009) 2297–2317.
[59] W.A. Brantley, Calculated elastic constants for stress problems associated with semiconductor devices, J. Appl. Phys. 44 (1973) 534.
[60] R. Ballarini, R.L. Mullen, Y. Yin, H. Kahn, S. Stemmer, A.H. Heuer, The fracture toughness of polysilicon microdevices: a first report, J. Mater. Res. 12 (1997) 915–922.
[61] I. Chasiotis, W.G. Knauss, The mechanical strength of polysilicon films: Part 2. Size effects associated with elliptical and circular perforations, J. Mech. Phys. Solids 51 (2003) 1551–1572.
[62] M. Neal, T. Belytschko, Explicit–explicit subcycling with non-integer time step ratios for structural dynamic systems, Comput. Struct. 31 (1989) 871–880.
[63] P. Smolinski, S. Sleith, T. Belytschko, Stability of an explicit multi-time step integration algorithm for linear structural dynamics equations, Comput. Mech. 18 (1996) 236–244.
[64] J. Daniel, The subcycled newmark algorithm, Comput. Mech. 20 (1997) 272–281.
[65] W. Daniel, A partial velocity approach to subcycling structural dynamics, Comput. Methods Appl. Mech. Engrg. 192 (2003) 375–394.